Carbohydrate Polymers 385 (2026) 125392

Contents lists available at ScienceDirect

Carbohydrate Polymers

journal homepage: www.elsevier.com/locate/carbpol

Antibacterial and cell-instructive chitosan/NeoNectin hydrogels crosslinked via click chemistry enable osteogenic differentiation within ultra-soft matrices

Daniel Cabrerizo-Aguado [a,b,h,1], Federica Barbugian [a,b,h,1], Maria-Pau Ginebra [a,b,c,d,h], Xinru Wang [e,f], David Baker [e,f,g], Jose Maria Manero [a,b,c,h], Jordi Guillem-Marti [a,b,c,h,*]

[a] Biomechanics, Biomaterials and Tissue Engineering, Department of Materials Science and Engineering, Universitat Politècnica de Catalunya · BarcelonaTech (UPC), Barcelona, 08019, Spain
[b] Barcelona Research Centre in Multiscale Science and Engineering, Universitat Politècnica de Catalunya · BarcelonaTech (UPC), Barcelona, 08019, Spain
[c] Centro de Investigación Biomédica en Red—Bioingeniería, Biomedicina y Nanomedicina (CIBER-BBN), Madrid, Spain
[d] Institute for Bioengineering of Catalonia (IBEC), The Barcelona Institute of Science and Technology, Barcelona, 08028, Spain
[e] Department of Biochemistry, University of Washington, Seattle, 98195, USA
[f] Institute for Protein Design, University of Washington, Seattle, 98195, USA
[g] Howard Hughes Medical Institute, University of Washington, Seattle, 98195, USA
[h] Institute for Research and Innovation in Health (IRIS), Universitat Politècnica de Catalunya · BarcelonaTech (UPC), Barcelona, 08019, Spain

ARTICLE INFO

Keywords:
Chitosan
De novo protein design
Hydrogel
SPAAC reaction

ABSTRACT

Hydrogels are attractive scaffolds for regenerative medicine, yet few systems combine robust mechanical performance, antimicrobial functionality, and controlled bioactivity. Here, we engineered chitosan-based hydrogels crosslinked via strain-promoted azide–alkyne cycloaddition (SPAAC) using 4-arm PEG-DBCO and functionalized with NeoNectin, a de novo–designed protein exhibiting subnanomolar affinity and high specificity for integrin α5β1. Rheological analysis confirmed stable hydrogel formation with an elastic modulus of ~0.1 kPa, within the physiological range of bone marrow and typically associated with maintenance of mesenchymal stem cells (MSCs) in an undifferentiated state, enabling evaluation of integrin-specific biochemical cues in an inhibitory mechanical environment. Antimicrobial assays confirmed intrinsic bactericidal activity against *Staphylococcus aureus* and *Pseudomonas aeruginosa*, mitigating infection risks associated with implantation. Encapsulated human MSCs maintained high viability across all groups, validating cytocompatibility of the SPAAC crosslinking. Importantly, only covalently immobilized NeoNectin promoted sustained proliferation, increased expression of osteogenic genes, and significantly enhanced alkaline phosphatase activity, despite the low stiffness of the hydrogel matrix. These findings demonstrate that α5β1-specific signaling can override mechanical cues and drive osteogenic differentiation within ultra-soft environments. Overall, NeoNectin-functionalized SPAAC hydrogels provide a multifunctional platform that integrates antimicrobial properties, mechanical stability, and cell-instructive signaling for bone regeneration and broader tissue engineering applications.

1. Introduction

Hydrogels are three-dimensional polymeric networks capable of retaining large amounts of water, thereby closely mimicking the extracellular matrix (ECM) and providing a physiologically supportive environment for cells (Tibbitt & Anseth, 2009). They can be derived from natural polymers, such as alginate, collagen, hyaluronic acid, or chitosan, all of which exhibit intrinsic biocompatibility and biodegradability (Zöller et al., 2025). These properties, together with their tunable mechanical properties, capacity for biochemical functionalization, and

* Corresponding author at: Biomechanics, Biomaterials and Tissue Engineering, Department of Materials Science and Engineering, Universitat Politècnica de Catalunya · BarcelonaTech (UPC), Barcelona, 08019, Spain.
E-mail address: jordi.guillem.marti@upc.edu (J. Guillem-Marti).
[1] These authors contributed equally to this work.

https://doi.org/10.1016/j.carbpol.2026.125392
Received 27 March 2026; Received in revised form 28 April 2026; Accepted 1 May 2026
Available online 2 May 2026

ability to control the release of bioactive molecules, make hydrogels attractive candidates for regenerative medicine. Their interconnected porous structure facilitates cellular infiltration, nutrient diffusion, and tissue integration further supporting the repair of tissues (Segneanu et al., 2025).

Among natural polymers, chitosan stands out due to its biocompatibility, biodegradability and ease of chemical modification (Hong et al., 2024). However, despite these advantages, chitosan-based hydrogels face two critical limitations. First, they often lack sufficient mechanical stability under physiological conditions, which can compromise their performance in vivo (Sajeev et al., 2025). Second, chitosan does not intrinsically present adhesive ligands, limiting its ability to drive specific cellular interactions (Rodrigues et al., 2012).

Non-covalent interactions within chitosan confer biocompatibility but result in limited stability in vivo, compromising the integrity of the hydrogel and restricting its applicability. In contrast, covalent crosslinking provides enhanced structural stability and controlled degradation, but frequently requires crosslinking agents, UV irradiation, or chemical initiators, which may introduce cytotoxic effects (Jiang et al., 2024; Nicolle et al., 2021). In this context, click chemistry has emerged as a powerful alternative, with the Strain-Promoted Azide–Alkyne Cycloaddition (SPAAC) reaction representing a particularly promising approach. SPAAC offers high specificity, biocompatibility, and rapid gelation under mild conditions without the need for catalysts or UV light, thereby ensuring safe and efficient hydrogel crosslinking (Fu et al., 2017; Hodgson et al., 2016; Madl et al., 2016). Its biorthogonal nature minimizes cytotoxicity and undesired side reactions, which is particularly advantageous for systems involving cell encapsulation (Fan et al., 2015; Han et al., 2018). Moreover, the tunability of the SPAAC reaction allows fine control over mechanical stiffness and degradability, while its rapid gelation kinetics, ranging from seconds to minutes, make it highly suitable for clinical applications requiring injectable or in situ-forming materials (Li & Xiong, 2022; Nealy et al., 2024; Truong et al., 2014). These combined features make the SPAAC reaction highly stable, reproducible, and well-suited to biomedical applications, laying the groundwork for innovative hydrogel-based strategies in regenerative medicine.

The second major limitation of chitosan and other hydrogel systems lies in their lack of cell-adhesive motifs (Freier et al., 2005). To overcome this, fibronectin (FN) and its Arg-Gly-Asp (RGD) sequence have traditionally been used to promote cell adhesion (Bellis, 2011). Nonetheless, the use of FN is hindered by production and stability challenges, while RGD peptides, although are easier to synthesize, lack integrin specificity and display limited efficacy in promoting consistent bone regeneration (Elmengaard et al., 2005; Patten & Wang, 2021). Recent advances in de novo protein design have enabled us to computationally develop a new class of α5β1-specific integrin binder, NeoNectin, capable of stabilizing the active conformation of the receptor. In contrast to FN and RGD, NeoNectin displays subnanomolar affinity and exceptional specificity toward integrin α5β1, significantly enhancing cell adhesion and spreading in vitro, and tissue integration in vivo. The small molecular size, high stability, ease of production, low manufacturing cost, and low immunogenicity make NeoNectin an ideal candidate for incorporation into functionalized hydrogel systems (Wang et al., 2025).

Many hydrogel systems developed for tissue engineering are intentionally designed with high stiffnesses to meet the surrounding tissue environment and to mechanically stimulate cell differentiation or functionality. However, when biochemical cues are incorporated they are often coupled to mechanical signals, making it difficult to distinguish their individual contributions to cell fate decisions. Bone marrow, the physiological niche of MSCs, is characterized by an environment with an elastic modulus in the sub-kPa range. Such soft environment is associated with the maintenance of MSCs in an undifferentiated state (Doherty-Boyd et al., 2025), whereas osteogenic differentiation is promoted by stiffer matrices. Designing hydrogels that mimic the soft mechanical properties of bone marrow therefore provides a valuable platform to investigate whether specific biochemical signals can direct stem cell differentiation overriding the inhibitory mechanical cues.

In this study, we aimed to develop a chitosan-based hydrogel with enhanced mechanical stability and bioactivity through SPAAC-mediated covalent crosslinking and functionalization with NeoNectin, a de novo–designed α5β1 integrin-binding protein. The system was engineered by azide modification of both chitosan and NeoNectin, followed by crosslinking with a cyclooctyne-functionalized 4-arm PEG. We hypothesized that stable, covalent presentation of NeoNectin within a soft chitosan network would enable sustained α5β1 engagement and direct mesenchymal stem cell (MSC) fate overriding the inhibitory mechanical cues. The resulting hydrogels were characterized physicochemically, mechanically, and biologically, including antimicrobial assays and MSCs encapsulation studies. Our results demonstrate that covalent NeoNectin incorporation enables stable network formation, preserves chitosan's antibacterial activity, and promotes MSC proliferation and early osteogenic differentiation, establishing a multifunctional hydrogel platform for bone and tissue regeneration.

2. Materials and methods

2.1. Protein purification

NeoNectin was produced and purified as previously described (Wang et al., 2025). Briefly, BL21 cells were transformed with a pET29b plasmid containing the NeoNectin sequence. Cells were cultured in Luria Broth (LB) supplemented with kanamycin overnight with shaking. Cells were then diluted 1:50 and allowed to grow until the culture reached the exponential growth phase. The cultures were then induced by adding 1-Isopropylthio-β-D-galactopyranoside (IPTG, ThermoScientific, R1171) to a final concentration of 1 mM and incubated for 3 additional hours. The culture was then sonicated in PBS with a tablet of protease and phosphatase inhibitors (ThermoScientific), centrifugated at 4 °C and then filtered. NeoNectin was purified using Ni-NTA HisPur™ columns (ThermoScientific). After eluting, the purified protein was dialyzed using a 3.5 kDa cellulose membrane against 25 mM Tris-HCl, 100 mM NaCl, pH 8.0 for 4 days. Monodispersity was checked by size exclusion chromatography (SEC, Cytiva) in the same buffer. Then, the dialyzed proteins were lyophilized (Noxair lyophilizer) and stored at −20 °C.

2.2. Polymer functionalization and hydrogel formation

To functionalize chitosan, 1 mmol of N_3-PEG_4-COOH (Tebubio) was dissolved in PBS pH 5.5 at room temperature. Then, 2 mmol of 1-etil-3-(3-dimetilaminopropil) carbodiimide (EDC) and N-Hydroxysuccinimide (NHS), both from Thermo Fisher Scientific, were added under gentle stirring for the reductive amination. In parallel, 0.5 mmol water soluble chitosan (Biosynth; molecular weight 10–100 kDa, degree of deacetylation 90%) was dissolved in PBS pH 5.5. After 45 min, the chitosan solution was added dropwise into the PEG-azide solution and the reaction was agitated overnight at room temperature on an orbital shaker. An additional 2 mmol of EDC and NHS solution was added, and the mixture was agitated for 4 h, followed by dialysis against 0.1 M NaCl in water using a 1 kDa cellulose membrane (Sigma Aldrich) for 1 day. The solution was then dialyzed against deionized water for 2 days. The obtained azidated chitosan (CH-N_3) was frozen using liquid nitrogen, lyophilized (Noxair lyophilizer), and stored at −20 °C.

To functionalize NeoNectin, 0.15 mmol N_3-PEG_4-COOH was dissolved in PBS pH 5.5 at room temperature. Then, 0.3 mmol EDC and NHS were added under gentle stirring. A total of 0.073 mmol of lyophilized powder of purified NeoNectin was dissolved in PBS pH 5.5. After 45 min, the NeoNectin solution was added dropwise into the PEG-azide solution and the reaction was agitated overnight at room temperature on an orbital shaker. An additional 0.3 mmol of EDC and NHS solution was added, and the mixture was agitated for 4 h, after which it was dialyzed against 0.1 M NaCl using a 3.5 kDa cellulose membrane for

1 day. Next, the solution was dialyzed against deionized water for 2 days. The obtained azidated NeoNectin ($NN{-}N_3$) was frozen using liquid nitrogen, lyophilized (Noxair lyophilizer), and stored at −20 °C.

To obtain crosslinked chitosan hydrogels (CHN_3), lyophilized CH-N_3 was dissolved in PBS at a concentration of 25 mg/mL containing 50 U/mL and 50 μg/mL of penicillin and streptomycin, respectively, for the cell culture experiments or without antibiotics for the bacteria experiments. Then, the solution was mixed with a 96 mg/mL solution of 4arm-PEG-dibenzocyclooctyne (4arm-PEG-DBCO, PEG CreativeWorks) to form the hydrogel.

To obtain the NeoNectin-containing hydrogels (CHN_3-NN and CHN_3-NNN_3), 1 mM of NeoNectin or azidated NeoNectin (NN-N_3) were added to a 25 mg/mL CHN_3 solution with or without antibiotics as defined for CHN_3. Then the dissolved solutions were mixed with a 96 mg/mL solution of 4arm-PEG-DBCO to form the hydrogel.

2.3. Hydrogel characterization

2.3.1. ^1H NMR

Spectra of chitosan, NeoNectin and their PEG-azidated derivatives were obtained with an Ascend 400 AVANCE III HD 500 MHz spectrometer (Brucker, USA) equipped with a 5-mm TCI cryogenic probe at 303 K. A total of 3.5 mg of each reagent was dissolved in 550 μL deuterated water (D_2O) with 0.05% tetramethylsilane (TMS). The spectra were acquired with presaturation of proton residual peak (HDO), using 128 scans, a 25-s relaxation delay, and 32 K time-domain points. Spectra were processed with the TopSpin software.

2.3.2. FT-ATR

Spectra of the chitosan, NeoNectin, their PEG-azidated derivatives, and the different hydrogel compositions (CHN_3, CHN_3-NN and CHN_3-NNN_3) were recorded in attenuated total reflection ATR mode using a Nicolet 6700 Smart Orbit spectrometer (Thermo Scientific). All the samples were coated onto a steel surface and points from different areas were analyzed. The absorbances of the samples and backgrounds were measured using 128 scans each. The spectral absorption data were collected in the range between 4000 and 675 cm^{-1} at a spectral resolution of 2.0 cm^{-1} and an 8.0 gain.

2.3.3. Inverting test tube

Hydrogels were formulated as explained above in a 2 mL eppendorf tube and allowed to gel for 5 min. Then, the tubes were turned upside down and images were acquired with a cell phone.

2.3.4. Swelling ratio and water content tests

Swelling tests were performed by immersing a 100 μL hydrogel drop in 3 mL of PBS at 37 °C and weighing the hydrogel at different time points. Experimentally, the swelling ratio at each time point was calculated using the following formula:

$$Swelling\ Ratio\ (SW) = \frac{W_{wet}(t) - W_{dry}}{W_{dry}} * 100\ (\%)$$

where $W_{wet}(t)$ is the weight of the swollen hydrogel at a specific time point and W_{dry} is the initial weight of the hydrogel.

For calculating the water content, the following formula was used:

$$Water\ Content\ (WC) = \frac{W_{wet}(t) - W_{dry}}{W_{wet}(t)} * 100\ (\%)$$

2.3.5. Hydrogel degradation test

After hydrogel formation (100 μL), samples were incubated in deionized water overnight at 37 °C to allow swelling and equilibration. Prior to the degradation assay, hydrogels were weighed to obtain the initial mass. Subsequently, samples were incubated in 3 mL of PBS containing collagenase (2 U/mL, Thermo Fisher Scientific) and lysozyme (1 mg/mL, Thermo Fisher Scientific). At each predetermined time point, the hydrogels were weighed and a newly prepared enzymatic solution was added. The percentage of mass loss was calculated according to the following equation:

$$Mass\ loss\ (ML) = \frac{M_0 - M\,(t)}{M_0} * 100\ (\%)$$

where M_0 corresponds to the hydrogel mass after overnight swelling (initial mass), and $M\,(t)$ is the hydrogel mass at each evaluated time point.

2.3.6. Rheological analysis

For each analysis, hydrogels were incubated overnight in deionized water to ensure complete swelling. Rheological measurements were performed using a Discovery Hybrid HR-2 Rheometer (TA Instruments). An amplitude sweep was first conducted to determine the linear viscoelastic (LVE) region. Based on these results, frequency sweeps ranging from 0.01 Hz to 10 Hz were carried out at a fixed strain of 1% to obtain the storage modulus (G'), loss modulus (G''), crossover strain and damping factor ($\tan\delta = G''/G'$). All measurements were performed at 25 °C on hydrogels fabricated to match a 20 mm rough parallel plate geometry with a fixed gap of 2300 μm. All data were analyzed with the Trios software.

2.3.7. Mechanical compression testing

Compression tests were conducted in axial mode under gap-controlled conditions at a constant displacement rate of approximately 2 $\mu m \cdot s^{-1}$ until a maximum strain of 60% was reached. Normal force and displacement were continuously recorded during the test. The Young's Modulus was calculated from the measured normal force divided by the initial cross-sectional area of the hydrogel, and strain was determined as the ratio between displacement and initial sample height. The compressive modulus was obtained from the slope of the linear region of the stress–strain curve (typically between 10% and 20% strain). Conditions, hydrogels geometry, data processing and instruments were the same as in rheological analysis.

2.3.8. Scanning electron microscopy (SEM)

SEM images were obtained for characterizing the surface and the cross-section of the hydrogels. To this end, hydrogels were frozen using liquid nitrogen and then lyophilized (Noxair lyophilizer). Before visualization, each sample was sputter-coated with an 11 nm Iridium layer. The morphology and topography of the hydrogels were characterized using a Phenom XL Desktop SEM (Phenom-World) at a voltage of 5 kV, operating at a working distance of 6 mm. The sizes of pores were quantified with the FIJI/ImageJ software.

2.3.9. Protein release

To evaluate the release of NeoNectin from the hydrogels (CHN_3-NN and CHN_3-NNN_3), the released protein was quantified using Pierce™ BCA Protein Assay Kit (Thermo Fisher) following manufacturer's instructions. Briefly, hydrogels were covered with miliQ water and at each timepoint water was aspirated, transferred to new well plates and incubated with BCA reagent for 30 min at 37 °C. The absorbance at 562 nm was recorded with an Infinite 200 PRO microplate reader (Tecan, Switzerland).

2.4. Biological characterization

2.4.1. Bacterial species and culture conditions

For bacterial viability studies, *Pseudomonas aeruginosa* (CECT, Spain) and *Staphylococcus aureus* (CCUG, Sweden) were grown on Luria Broth (LB, Invitrogen) or Brain-Heart Infusion (BHI, Scharlab) medium, respectively. Inoculi from these bacteria were incubated at 37 °C until the optical density (OD_{600}) reached a value of 0.2, which corresponds to

approximately 1 × 10^8 colony forming units (CFU)/mL.

2.4.2. Bacterial viability on hydrogels

A drop of 50 μL of CHN_3, CHN_3-NN or CHN_3-NNN_3 was deposited on a μ-slide 8 well high glass bottom chamber (Ibidi) and covered with 200 μL of an inoculum of *P. aeruginosa* or *S. aureus*. Hydrogels were then incubated for 6 h at 37 °C. The samples were rinsed three times with PBS to remove non-attached bacteria, and attached bacteria were fixed in 2.5% (v/v) glutaraldehyde in PBS for 30 min at room temperature. The hydrogels were then washed three times with PBS and incubated with the fluorescent dye mixture of the Live/Dead BacLight™ Bacterial Viability Kit (Invitrogen), following the supplier's instructions. Images were acquired in an LSM 800 (Carl Zeiss, Germany), and processed and analyzed using the FIJI/ImageJ software. The number of living (green) and dead (red) bacteria were calculated. Bacteria seeded directly on the glass of the chamber were used as control.

2.4.3. Inhibition zone

A 200 μL bacterial suspension was spread on LB or BHI agar plates. Then, 15 mm hydrogels previously incubated in deionized water for 24 h were placed on top of the agar plates. The plates were incubated for 24 h at 37 °C. The diameter of the growth inhibition halo was measured using a ruler with FIJI/ImageJ software.

2.4.4. Cell culture and maintenance

Human bone marrow MSC (ATTC) were cultured in Advanced DMEM medium supplemented with 10% fetal bovine serum (FBS), 20 mM HEPES, 2 mM L-Glutamine, and 50 μg/mL penicillin/streptomycin (all components from Gibco). The cells were maintained at 37 °C in a humidified atmosphere and 5% CO_2. In all the experiments, cells from passage 5 were used and encapsulated at a density of 75,000 cells/mL in complete medium supplemented with 3% FBS medium.

2.4.5. Indirect cytotoxicity

Hydrogel drops were incubated with Advanced DMEM for 48 h at 37 °C and 5% CO_2. Then, the medium was transferred to a new well containing 10,000 attached MSCs. Cells were incubated for 24 h, and medium was replaced with a new medium containing 10% of Presto Blue cell viability reagent (Invitrogen). After 1 h at 37 °C, the solution was transferred to a black 96-well plate and fluorescence was measured (λ_{ex} = 560 nm, λ_{em} = 590 nm) using an Infinite 200 PRO microplate reader. The percentage of viable cells was determined by comparison with MSCs incubated in complete medium in the absence of hydrogels.

2.4.6. Hydrogel formulation with embedded cells

MSCs were centrifuged and resuspended in PBS containing CH-N_3 with or without NN-N_3 or NeoNectin alone. Then, PBS containing 4arm-PEG-DBCO was added and mixed homogeneously before dropping 50 μL in a μ-slide 8 well high glass bottom chamber. After 30 min of incubation at 37 °C, 200 μL/well of complete Advanced DMEM was added, incubating the hydrogels for 7 days at 37 °C, in a humidified atmosphere and 5% CO_2. The media was changed every other day.

2.4.7. MSCs viability inside the hydrogels

The viability of MSCs embedded in the hydrogels was evaluated using a Live/Dead stain kit (Thermo Fisher Scientific) following the manufacturer's instructions. After 1, 3 and 7 days in culture, the media was removed and the hydrogels were incubated in 2 μM Calcein-AM and 4 μM ethidium homodimer-1 for 30 min at 37 °C. Stained hydrogels were washed two times with PBS before imaging in an LSM 800 confocal microscope. Images were processed and analyzed using the FIJI/ImageJ software. The number of living (green) and dead (red) MSCs were calculated from at least 4 randomly selected areas.

2.4.8. MSCs spreading inside the hydrogels

Cells embedded in the hydrogels were stained after 1, 3 and 7 days of culture for morphological analysis. In detail, the medium was removed, and the hydrogels were fixed at room temperature for 20 min using a 4% paraformaldehyde solution. Then the hydrogels were incubated with 0.5% triton X-100 for 15 min and blocked with 1% BSA for 30 min. Finally, the samples were stained with Alexa Fluor 546 Phalloidin (1:100, Invitrogen) for 1 h, followed by incubation with DAPI (1:1000, Invitrogen) for 5 min. The hydrogels were washed thrice with PBS between each step. Images were acquired in an LSM 800 confocal microscope. The circularity of MSCs was calculated in at least 30 randomly selected cells using the FIJI/ImageJ software.

2.4.9. MSCs proliferation inside the hydrogels

The number of cells inside the hydrogels was quantified after 1, 3 and 7 days of incubation. At each time point, cells were released by incubating the hydrogels for 1 h at 37 °C in 2 U/mL chitosanase (Sigma-Aldrich) diluted in 50 mM sodium acetate, 0.9% w/v NaCl pH 5.5. During the incubation, the solution was pipetted several times to ensure complete destruction of the hydrogels. The resulting solution was then centrifuged and the cell pellet was resuspended in mammalian protein extraction reagent (M-PER, Fisher Scientific). The lactate dehydrogenase (LDH) activity was quantified using the Cytotoxicity Detection KitPLUS (LDH) (Roche - 4744934001) following manufacturer's indications. Absorbance was recorded at 492 nm with an Infinite 200 PRO microplate reader. The number of cells was extrapolated from a curve obtained with increasing number of MSCs cultured on tissue culture polystyrene. The proliferation fold change was calculated by dividing the number of cells of each condition to the number of cells obtained in the CHN3 hydrogel at day 1.

2.4.10. MSCs gene expression inside the hydrogels

After 3 and 7 days of culture, the expression of osteogenic-related genes was analyzed by quantitative reverse transcription polymerase chain reaction (RT-qPCR). At each time point, samples were washed with PBS for 15 min at 37 °C and total RNA was isolated using TRIzol Reagent (Invitrogen) according to the manufacturer's instructions, with minor modifications. Briefly, 1 mL of TRIzol was added to each sample and incubated for 20 min at room temperature under shaking conditions. Then phase separation was induced by adding 0.2 mL of chloroform. Samples were vigorously mixed and incubated for 3 min at room temperature, followed by centrifugation at 12,000 ×*g* for 15 min at 4 °C. The upper aqueous phase containing RNA was carefully collected and transferred to a new tube, and the same volume of 70% ethanol was added. RNA purification was subsequently completed using RNeasy Mini Kit columns (Qiagen), following the manufacturer's protocol. RNA concentration was determined using a nanodrop Nano-400A (Allsheng) The purified RNA was stored at −80 °C until further use. Complementary DNA (cDNA) was synthesized using Maxima First Strand cDNA (Thermo Scientific). Prior to reverse transcription, the RNA was treated with dsDNase to remove remnants of genomic DNA from the previous purification. RT-qPCR was performed using AriaMx Real-Time PCR System (Agilent) with the QuantiFast SYBR Green PCR Kit (Qiagen). β-Actin was employed as the housekeeping gene, and relative gene expression was calculated using the $2^{-\Delta\Delta Ct}$ method using hMSCs cultivated in 2D in polystyrene at the same timepoints. Primer sequences are listed in Table 1.

Table 1
List of primer sequences used in RT-qPCR.

Gene	Forward primer	Reverse primer
β-Actin	CCACCATGTACCCTGGCATT	GTACTTGCGCTCAGGAGGAG
ALP	AGAACCCCAAAGGCTTCTTC	CTTGGCTTTTCCTTCATGGT
BMP-2	CAGACCACCGGTTGGAGA	CCCACTCGTTTCTGGTAGTTCT
DLX5	GTGAGCGATGACAGGAGTGT	TGGAACGGAGCTTGGAAGTC
OCN	CACACTCCTCGCCCTATTGG	CTTGGACACAAAGGCTGCAC
RUNX2	CGGAATGCCTCTGCTGTTAT	TGGGGAGGATTTGTGAAGAC
SP7	GTGGGAAATAGTGGGCAGCT	TGCCCCCATATCCACCACTA

2.4.11. MSCs alkaline phosphatase (ALP) expression inside the hydrogels

The ALP activity was measured as an indicator of cell differentiation. MSCs were incubated for 1, 3 and 7 days inside the hydrogels and the same extract from the proliferation experiment was used for ALP quantification. The lysate was incubated for 60 min at 37 °C with the reagents from the SensoLyte pNPP Alkaline Phosphatase Activity Kit (AnaSpec). ALP activity was quantified by measuring the absorbance at 405 nm using an Infinite 200 PRO microplate reader. ALP values were normalized to the cell content of each sample obtained in the proliferation assay.

2.5. Statistical analysis

All data are presented as mean ± SD. Statistical significance was determined using a one-way analysis of variance (ANOVA) followed by Tukey's Post-hoc Test. Differences were considered statistically significant when $p < 0.05$ (*), $p < 0.01$ (**), $p < 0.001$ (***), and $p < 0.0001$ (****).

3. Results and discussion

3.1. Chemical modification of the hydrogel components

Chitosan and NeoNectin were functionalized with N_3-PEG_4-COOH via carbodiimide chemistry to obtain the PEG-azidated derivatives (Ikeda, 2018). To achieve this, we first activated the carboxylic acid group of N_3-PEG_4-COOH, using EDC in the presence of NHS (Rayamajhi & Aryal, 2020). This process resulted in an active ester intermediate, which subsequently reacts with the primary amines of chitosan or NeoNectin, forming stable amide bonds (Tang et al., 2020). The successful functionalization of chitosan and NeoNectin with PEG_4-N_3 was corroborated by NMR and FT-ATR spectroscopy.

For chitosan, the NMR spectrum showed a signal at 2 ppm (yellow region, Fig. 1A) corresponding to the methyl protons of the *N*-acetyl groups (Dong et al., 2026). Following azide functionalization (CH-N_3), a broad multiplet appeared at 3.4–4.2 ppm (green region), attributable to both the sugar-ring protons and the $-CH_2$ protons adjacent to the PEG

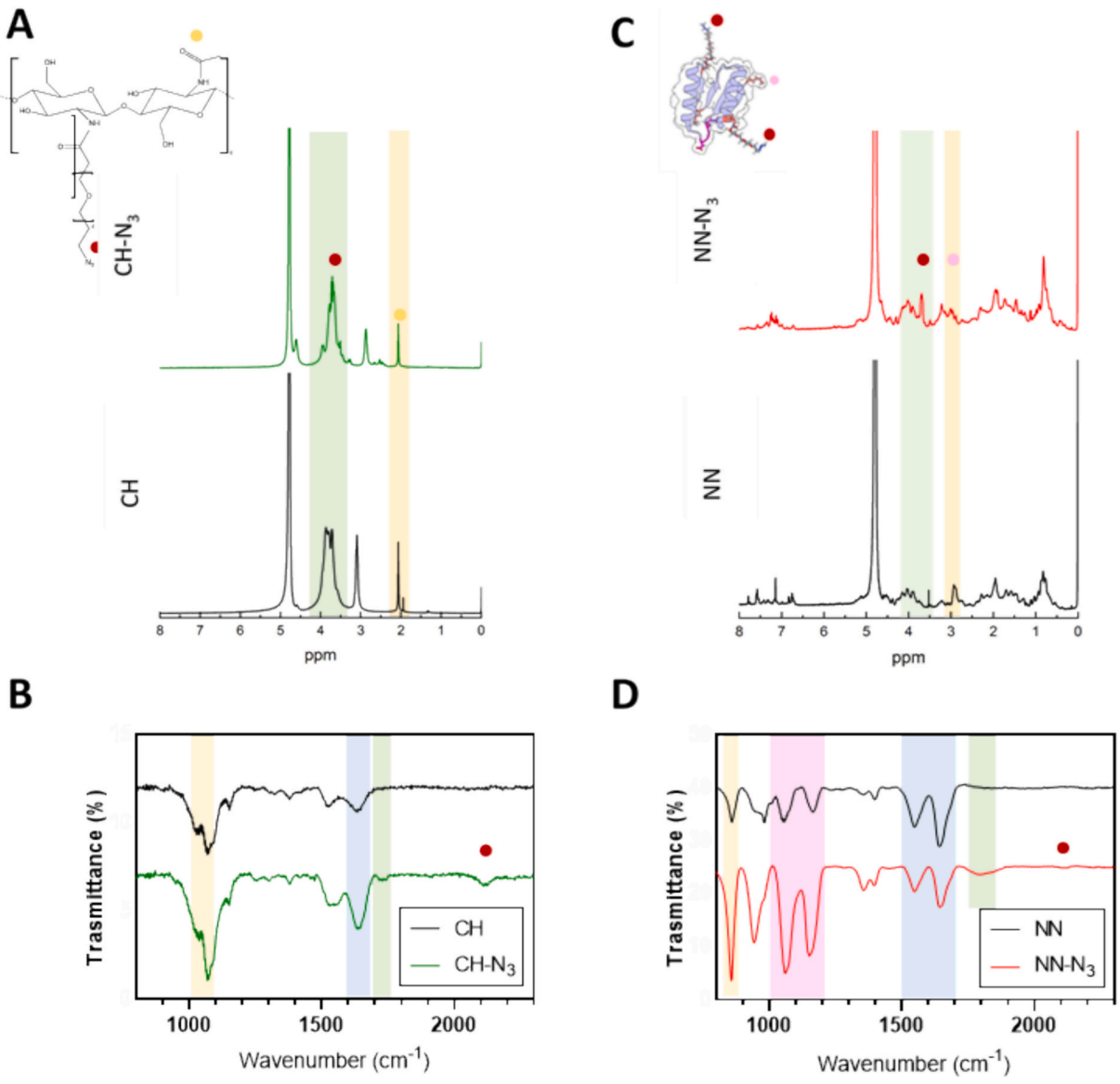

Fig. 1. ^{1}H NMR spectra of (A) chitosan (CH, bottom) compared to azidated-chitosan (CH-N_3, top), and (B) NeoNectin (NN, bottom in black) compared to azidated-NeoNectin (NN-N_3, top in green). The azide groups are highlighted as red circles while the free amine and the *N*-acetyl group are highlighted as pink and yellow circles, respectively. FT-ATR of (C) CH compared to CH-N_3, and (D) NN compared to NNN_3. (For interpretation of the references to color in this figure legend, the reader is referred to the web version of this article.)

chain oxygen (Li et al., 2025). The degree of functionalization, calculated by comparing the integrated areas of the *N*-acetyl group and the 3.4–4.2 ppm multiplet, was 21.6 ± 4.8% (n = 10). FT-ATR analysis further supported successful functionalization of chitosan (Fig. 1B). The spectrum displayed changes in the amide I band 1630 cm^{-1} (blue region) consistent with formation of new amide linkages upon PEG-N_3 coupling (Gómez-Fernández and Villalaín, 1998), while an intensified band at 1725 cm^{-1} (green region) reflected the carbonyl-containing groups introduced by the PEG-N_3 (Sizeland et al., 2018). These two bands demonstrate that the PEG chains were covalently attached to the chitosan backbone. The slight change in the 1000–1100 cm^{-1} (yellow region) peak can be attributed to C═O and C—O stretching of the polysaccharide backbone due to alterations in hydrogen-bonding and chain packing caused by functionalization (Huynh et al., 2013). Notably, a band at 2150 cm^{-1} (red point) characteristic of the azide functional group (Liu & Chung, 2016) was observed only in CH-N_3. Together, these spectral changes, especially the enhanced amide and C—N bands provide direct chemical evidence of PEG incorporation, complementing the NMR findings and confirming that chitosan was successfully functionalized.

For NeoNectin, the control NMR spectrum displayed a resonance at 2.9–3.0 ppm (yellow region, pink marker, Fig. 1B) characteristic of the methylene protons of lysine side chains. (Stagi et al., 2022). After PEG_4-N_3 modification (NN-N_3), this signal decreased notably, indicating conversion of lysine free amines into amide linkages (Hagan et al., 2010). In parallel, the broad multiplet between 3.5 and 4.2 ppm exhibited an increase at approximately 3.6 ppm (green region, red marker), consistent with the $-CH_2$ protons of the PEG chain (Li et al., 2025). Together, the loss of the lysine-amine peak and the presence of PEG-associated signals provide direct evidence that PEG_4-N_3 moieties were covalently attached to NeoNectin. Because of the inherent complexity of the ^{1}H NMR spectra and the absence of an internal reference peak in the control protein spectra, it was not possible to quantify the exact degree of functionalization. Nonetheless, the qualitative spectral changes strongly support efficient conjugation. Furthermore, the FT-ATR spectrum of functionalized NeoNectin showed increased intensity at 1100 and 880 cm^{-1} (pink and yellow regions), characteristic of C—O stretching (Ji et al., 2020). Additional variations were observed at 1650 and 1550 cm^{-1} (blue region), corresponding to shifts in the amide II and amide I bands, respectively, which reflect changes in the protein backbone upon conjugation (Genshaft et al., 2013). The band at 1725 cm^{-1} (green region) reflected the carbonyl-containing groups present in the PEG-N_3 (Sizeland et al., 2018). Importantly, an absorption at 2150 cm^{-1} (red point) was detected, characteristic of the azide functional group (Liu & Chung, 2016). Together, these spectral features, especially the azide peak and the enhanced C—O and amide bands, further corroborate the successful PEG_4-N_3 functionalization of NeoNectin.

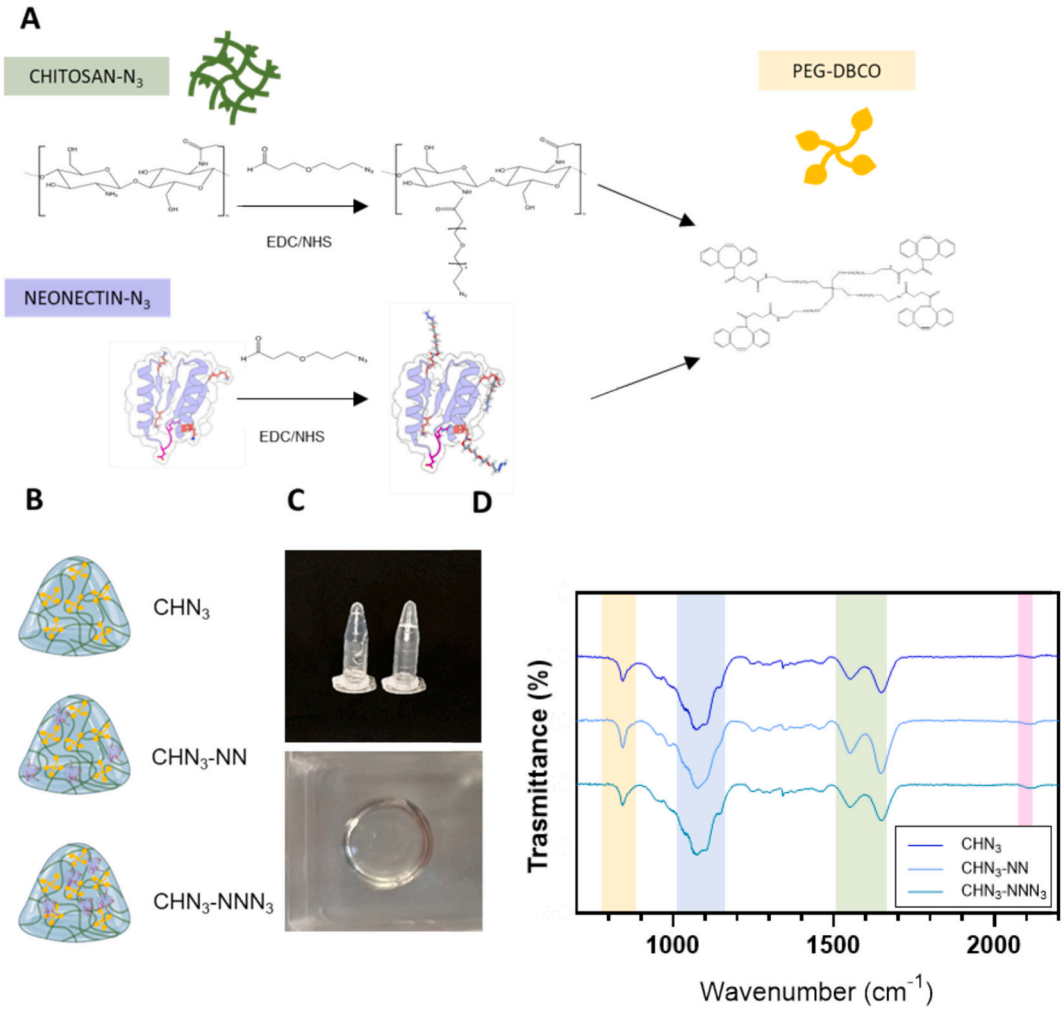

Fig. 2. (A) Schematic representation of the azidation of chitosan and NeoNectin, and functionalization with 4-arm PEG-DBCO. (B) Schematic structure of the chitosan (CHN_3), chitosan crosslinked with non-azidated NeoNectin (CHN_3-NN) and chitosan crosslinked with azidated NeoNectin (CHN_3-NNN_3) hydrogels. (C) Inverting test tube showing gel formation (top) and hydrogel drop formed (bottom). (D) FT-ATR of the different hydrogels.

3.2. Hydrogel formation

The PEG-azidated derivatives of chitosan and NeoNectin were combined with a 4-arm PEG bearing DBCO groups on each arm to achieve covalent crosslinking of the hydrogel (Fig. 2A and B). This linker was chosen to provide substantial spatial freedom within the network, thereby supporting cell viability during gelation (Kwon et al., 2021). Once the components were mixed, the SPAAC reaction proceeded spontaneously, without the need for additional reagents or catalysts. The high density of amine groups along the chitosan backbone and the three available lysine residues in NeoNectin (Fig. 2A) contributed to rapid network formation, with gelation occurring within 30 s (Fig. 2C).

To optimize the final formulation, we performed preliminary experiments assessing hydrogel stability, viscosity, gelation time and cell viability across a range of component concentrations (Table S1). The formulation that exhibited the greatest stability in aqueous conditions, resisting premature collapse, while displaying fast gelation time was selected for subsequent studies. This optimized hydrogel contained chitosan, NeoNectin, and 4-arm PEG-DBCO in a 1:14:5 ratio. In contrast, the same mixture prepared with non-azidated chitosan and NeoNectin failed to form a gel, underscoring the necessity of azide functionalization. The flexibility of the 4-arm PEG and the position of the lysines that were functionalized, which are opposite to the RGD loop of NeoNectin (Fig. 2A, lysines in red and RGD in pink) ensures correct presentation to α5β1 integrin. According to our previous study, the chosen concentration of 1 mM was sufficient to produce a high response in hMSCs (Wang et al., 2025).

Successful crosslinking of all components with the 4-arm PEG-DBCO

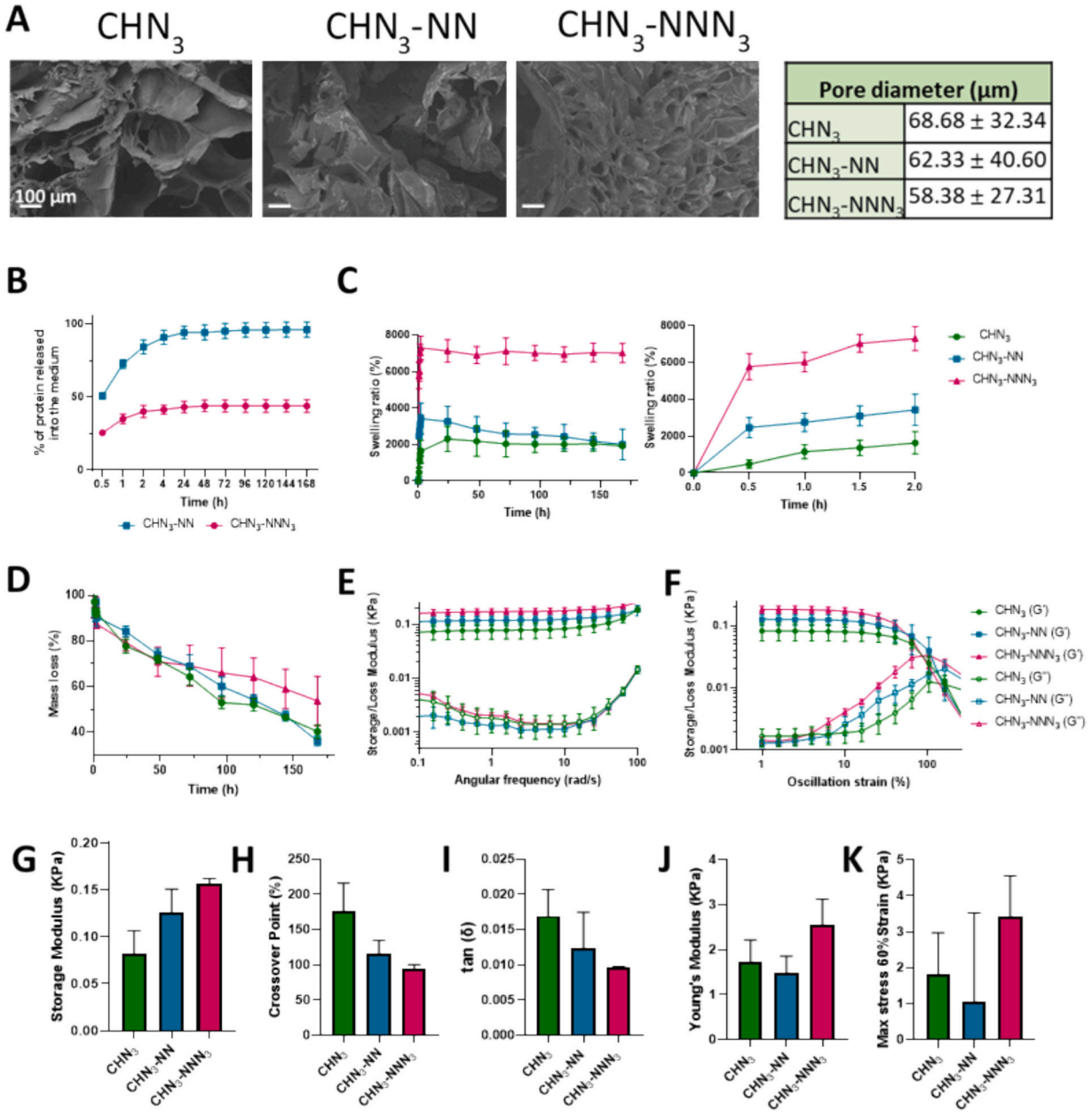

Fig. 3. Characterization of chitosan-based hydrogels. (A) SEM micrographs of the freeze-dried hydrogels and corresponding pore-size quantification. (B) Protein release profiles measured by BCA assay over one week. (C) Swelling ratio of the hydrogels during 1 week upon PBS immersion (left) and magnified view of the first 2 h (right). (D) Degradation test of the hydrogels during 1 week upon enzymatic cocktail. (E) Amplitude sweep showing the evolution of storage (G′) and loss (G″) modulus. (F) Frequency sweep curves within the linear viscoelastic region (1% strain). (G) Quantified storage modulus (G′). (H) Crossover strain. (I) Damping factor (tan δ). (J) Young's Modulus. (K) Maximum stress at 60% strain.

was verified by FT-ATR spectroscopy (Fig. 2D). Spectra of the chitosan hydrogel containing crosslinked NeoNectin (CHN_3-NNN_3) were compared with controls containing a non-azidated version of NeoNectin (CHN_3-NN) or lacking NeoNectin (CHN_3). In all conditions, the broad band at 1080–1150 cm^{-1} (blue region) corresponded to the C═O from PEG (Ramya et al., 2024). The azide stretch at 2100–2150 cm^{-1} (pink region), observed in the functionalized chitosan (Fig. 1C) was substantially reduced after SPAAC, which is consistent with azide consumption and triazole formation. Finally, the C—H vibrations at 750 cm^{-1} (yellow region) can be attributed to presence of cyclic compounds (Ai et al., 2017), in special those containing aromatic substituents. These signals confirm the presence of the DBCO-mediated triazole linkages and thus the effective covalent incorporation of all components within the hydrogel network. Bands of triazole linkage, which contains C—N and C═N, overlapped with C═O from PEG (blue region) at 1200–1350 cm^{-1} complicating their identification. Similarly, protein incorporation in CHN_3-NN and CHN_3-NNN_3 could not be confirmed with FT-ATR because amide I and II bands (green region, 1500–1650 cm^{-1}) overlapped with the amide bands of chitosan.

3.3. Mechanical properties of the hydrogels

The structural and mechanical properties of the hydrogels were analyzed to elucidate the relationship between network architecture, protein retention, and viscoelastic behavior. SEM imaging (Fig. 3A) revealed highly porous, interconnected microstructures typical of freeze-dried hydrogels. Quantitative pore analysis showed a similar average pore size in all the formulations with no statistical differences but a slight decreasing size tendency with functionalization (CHN_3 > CHN_3–NN > CHN_3–NNN_3), consistent with denser network formation and more uniform crosslink distribution in the covalently linked system. These results indicate that the covalent incorporation of NeoNectin promotes a more homogeneous and cohesive network architecture, likely improving mechanical integrity and long-term stability.

Azidation of NeoNectin before the SPAAC reaction significantly slowed its release from the hydrogel (Fig. 3B). In CHN_3–NN hydrogels, which contain non-functionalized NeoNectin, roughly 50% of the protein was released within the first 30 min, reaching a cumulative release of nearly 95% by 48 h. This profile reflects a classic burst release occurring by diffusion of non-immobilized protein through the hydrogel pores (Delgado et al., 2002). The relatively more open porosity of CHN_3–NN hydrogel also contributed to a faster release. In contrast, CHN_3–NNN_3 hydrogels exhibited a more sustained protein release, with only about 25% released during the initial 30 min and approximately 45% after 48 h, remaining stable for at least 7 days. This slower profile is a direct consequence of the protein functionalization, which limits protein mobility and minimizes the initial burst. Incomplete retention can be attributed to two factors. First, functionalization of NeoNectin is unlikely to reach complete efficiency; consequently, a fraction of non-functionalized proteins would diffuse freely although at a lower rate than in CHN_3–NN hydrogels. Second, azidated chitosan competes with azidated NeoNectin for DBCO sites during the SPAAC reaction, which could leave a fraction of functionalized NeoNectin susceptible to diffusion. Such findings confirm that azide functionalization efficiently regulates protein retention within the hydrogel network. A schematic representation of the burst versus sustained release observed in CHN_3-NN and CHN_3-NNN_3 formulations, respectively, can be visualized in Fig. S1.

The swelling behavior and water content (Figs. 3C and S2) provided further insight into the network organization and stability of the hydrogels. All samples exhibited a rapid initial water uptake, typical of hydrogel systems where solvent diffusion is initially faster than polymer chain relaxation, followed by a plateau as equilibrium was reached (Cheng et al., 2017). While CHN_3 and CHN_3–NNN_3 maintained relatively stable swelling ratios over time, CHN_3–NN showed a progressive decrease in swelling capacity after 48–72 h. This decline suggests partial network relaxation or collapse, likely due to the physical release of NeoNectin molecules that were initially trapped within the matrix but not covalently bound. The presence of these mobile NeoNectin during gelation may have introduced local heterogeneities and looser regions that reorganize over time as the protein diffuses out, leading to gradual loss of water-holding capacity (Branco et al., 2010). In contrast, CHN_3–NNN_3 reached the highest equilibrium swelling ratio and maintained it consistently throughout the experiment. This behavior can be attributed to the charged surface residues of covalently grafted NeoNectin, which enhance electrostatic interactions with surrounding water molecules without compromising network integrity. This is consistent with previous findings on covalently functionalized chitosan and PEG hydrogels (Chang et al., 2016). The increased hydration capacity, combined with a stable covalent network, enables CHN_3–NNN_3 to swell extensively while preserving mechanical cohesion and dimensional stability. Meanwhile, the unmodified CHN_3 hydrogel displayed a moderate but steady swelling behavior, consistent with its simpler and more homogeneous crosslinked architecture. Overall, these results highlight that the mode of protein incorporation, physical versus covalent, profoundly affects the water uptake dynamics and long-term structural stability of chitosan-based hydrogels.

The enzymatic degradation of the hydrogels was evaluated by monitoring mass loss over time in the presence of collagenase and lysozyme (Fig. 3D). All formulations exhibited progressive degradation, although distinct kinetics were observed among conditions. These results indicate that increasing network functionalization enhances hydrogel stability against enzymatic breakdown, likely by limiting enzyme accessibility within the network. From a tissue engineering perspective, controlled degradation is essential for bone regeneration, where scaffolds must provide temporary mechanical support while allowing progressive matrix remodeling and cell infiltration. The tunable degradation profiles observed here therefore support the suitability of these hydrogels as dynamically remodelable matrices for bone-related applications (Khetan & Burdick, 2011).

Rheological analysis (Fig. 3E–F) confirmed that all hydrogels exhibited the characteristic mechanical fingerprint of crosslinked polymeric networks: a predominantly elastic behavior at small deformations, with storage modulus (G') exceeding loss modulus (G'') across the frequency range, and a transition to viscous flow beyond the linear viscoelastic (LVE) regime (Stojkov et al., 2021). These profiles confirm the formation of crosslinked, water-swollen polymeric networks, in which the balance between elasticity and viscosity is governed by the number and density of crosslinks (Lv et al., 2019).

Amplitude sweep experiments revealed that all hydrogels possessed a well-defined LVE region, followed by network failure at higher strains. Frequency sweeps within the LVE (1% strain) confirmed the predominance of elastic behavior, with G' remaining relatively constant over the tested frequencies. This elastic response can be attributed to the presence of PEG chains covalently linked to chitosan, which introduce flexibility to the network while maintaining structural integrity (Tsao et al., 2015). Among the three formulations, CHN_3–NNN_3 exhibited a slightly higher mean G' (Fig. 3G), consistent with the introduction of additional anchoring sites for the DBCO crosslinker through azide-modified NeoNectin. However, the differences were not statistically significant across conditions, indicating that the incorporation of the protein did not substantially alter the overall stiffness of the network. The modest trend toward higher G' likely reflects minor local reinforcement due to increased crosslinking density (Boni & Regan, 2023), but all hydrogels remain within the same viscoelastic range, allowing the decoupling of mechanical and biochemical effects in subsequent biological assays.

The crossover strain and damping factor (Fig. 3H and I) provided further insight into the mechanical behavior of the crosslinked hydrogels. The CHN_3–NNN_3 formulation exhibited both the lowest crossover strain and the lowest damping factor (tan δ), indicating that it behaves as an elastic and cohesive material (Rolón-Garrido & Wagner, 2009).

This result suggests that CHN_3–NNN_3 hydrogel efficiently stores mechanical energy and resists viscous deformation under small stresses, although it becomes stiffer and less deformable when subjected to larger strains. Such behavior is characteristic of tightly crosslinked hydrogels (Day et al., 2025), where increased rigidity often reduces deformability. In contrast, CHN_3–NN and CHN_3 showed higher crossover points and damping factors, suggesting softer and more energy-dissipative networks. Altogether, all hydrogel formulations exhibited comparable viscoelastic behavior within the range suitable for physiological stability. CHN_3–NNN_3 showed a minor but non-significant increase in elastic response, consistent with its slightly denser crosslinking, yet without altering the overall mechanical profile of the system. These rheological observations support the of increased stiffness and reduced viscous behavior observed as well in the microstructural compaction.

To further characterize the bulk mechanical response under compressive loading, unconfined axial compression tests were performed and the Young's modulus was calculated from the linear region of the stress–strain curves (10–20% strain) (Fig. 3J). All hydrogels exhibited Young's modulus values within the low kilopascal range, confirming their soft and highly hydrated nature. CHN_3 showed a modulus of 1.7 kPa, while CHN_3–NN presented slightly lower values (1.5 kPa). CHN_3–NNN_3 displayed the highest mean modulus (2.5 kPa), suggesting a moderate reinforcement of the network when NeoNectin was covalently incorporated. However, no statistically significant

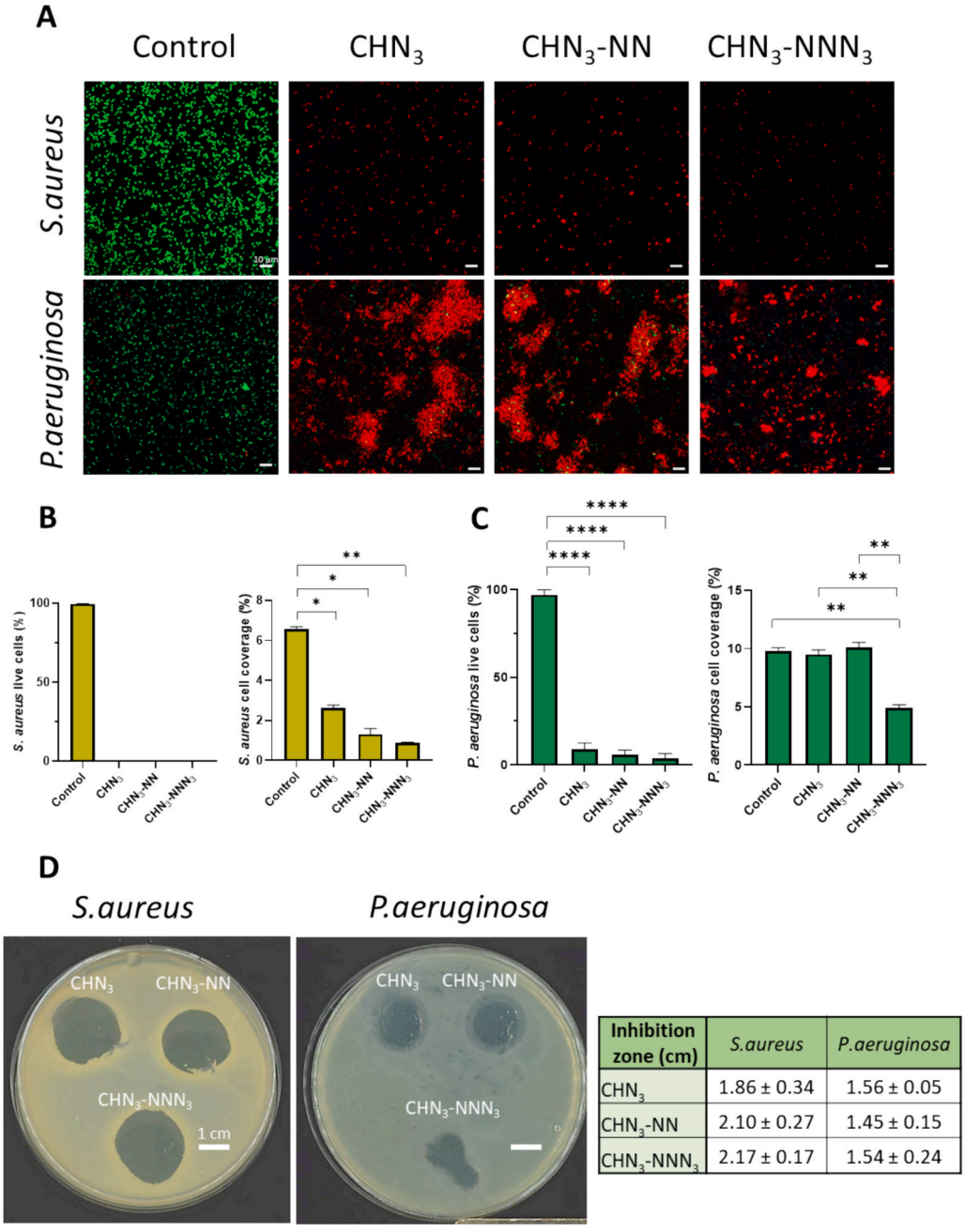

Inhibition zone (cm)	*S.aureus*	*P.aeruginosa*
CHN_3	1.86 ± 0.34	1.56 ± 0.05
CHN_3-NN	2.10 ± 0.27	1.45 ± 0.15
CHN_3-NNN_3	2.17 ± 0.17	1.54 ± 0.24

Fig. 4. Antibacterial properties of the hydrogels after 6 h of incubation. (A) Live/dead staining of *S. aureus* (top) and *P. aeruginosa* (bottom). Living cells are stained in green and dead cells are stained in red. Scale bar denotes 10 µm. (B) Quantification of the percentage of living cells (left) and the percentage of area covered by cells (right) based on the Live/dead staining for *S. aureus.* (C) Quantification of the percentage of living cells (left) and the percentage of area covered by cells (right) based on the Live/dead staining for *P. aeruginosa.* (D) Inhibition zone in agar plate (left) and calculated halo diameter (table). Scale bar denotes 1 cm. (For interpretation of the references to color in this figure legend, the reader is referred to the web version of this article.)

differences were detected among the three formulations. The slight increase observed in CHN_3–NNN_3 is consistent with the rheological trends and may reflect additional covalent anchoring points introduced by azidated NeoNectin during SPAAC crosslinking. Consistently, CHN_3–NNN_3 reached higher stress values across the strain range and showed the highest maximum stress at 60% strain (Fig. 3K), although again without statistical significance. Overall, all hydrogels remained within the same stiffness range (0.1–0.15 kPa), indicating a comparable mechanical environment across conditions. In fact, the stiffness of the hydrogels designed in the present study is within the range of the physiological bone marrow (0.1–10 kPa) (Doherty-Boyd et al., 2025; Donnelly et al., 2024), where MSCs should maintain their undifferentiated state, supporting that the biological differences should not be primarily driven by variations in bulk stiffness. Specifically, maintaining MSCs on such soft, bone marrow-mimetic substrates has been shown to effectively delay cellular senescence by modulating redox homeostasis and mitigating excessive cytoskeletal tension (Kuboki & Kidoaki, 2025). This preservation of a youthful phenotype is crucial for clinical applications, as mechanical rejuvenation of senescent stem cells (through the restoration of intracellular forces and chromatin remodeling) has been demonstrated to directly counteract age-related bone loss and improve skeletal integrity (Liu et al., 2026). Thus, the ultra-soft nature of our CH/NN hydrogels not only supports the maintenance of stemness but may also provide a protective environment against the functional decline associated with MSC aging.

3.4. Antibacterial activity

The antibacterial properties of the functionalized hydrogels were evaluated against *P. aeruginosa* and *S. aureus*, chosen as representative Gram-negative and Gram-positive bacteria species commonly found on human skin and implicated in peri-implant infections and implant failure. We observed high levels of bacterial death in both species in all the hydrogels (Fig. 4A). Specifically, more than 90% of *P. aeruginosa* were non-viable, while complete bacterial death was detected for *S. aureus*. No significant differences were detected among the different hydrogel compositions. This potent antibacterial activity is mainly attributed to the cationic nature of chitosan at acidic to neutral pH, where protonated amine groups ($–NH_3^+$) electrostatically interact with negatively charged bacterial membranes (Ke et al., 2021). Similar to cationic antimicrobial peptides, this interaction disrupts membrane integrity, leading to leakage of intracellular contents and cell death (Huan et al., 2020). The slight differences between the Gram-negative and Gram-positive bacteria observed in the present study should be attributed to their differences in their wall architecture. *S. aureus* are gram-positive bacteria that possess a thick and porous peptidoglycan layer enriched with negatively charged teichoic acids, which allows electrostatic interaction with chitosan. In contrast, the presence of an outer membrane rich in lipopolysaccharides provides partial protection to *P. aeruginosa* (Sutton et al., 2021).

The relatively high concentration of chitosan used here (2.5%) likely reinforced the antibacterial activity, consistent with reports that chitosan's antimicrobial activity is dose-dependent (Kovács et al., 2022). Increasing the density of protonated amine groups leads to greater electrostatic disruption of bacterial membranes. Drápalová et al. previously observed that increasing chitosan concentrations in hydrogels significantly reduces bacterial growth, with maximum effects at 1% concentration (Drápalová et al., 2023). We used higher concentrations of chitosan to both ensure structural stability of the hydrogels (Table S1) and to maintain the high-charge density required for bactericidal effects, considering a potential reduction of available protonated amine groups after crosslinking and NeoNectin functionalization. Noteworthy, the PEG-azide functionalization did not affect the bactericidal efficacy. Since the degree of functionalization was roughly 21%, a substantial number of amine groups in chitosan remained available for protonation, maintaining an effective bactericidal action. The presence of NeoNectin in the hydrogels did not alter bacterial viability under these conditions.

It is also important to mention that bacterial attachment to the hydrogel was low, being this effect more pronounced in *S. aureus* (Fig. 4B). This behavior could be explained by the tendency of *P. aeruginosa* to form biofilms in some surfaces (Thi et al., 2020), as we observed aggregates of bacteria on the hydrogels although the total area covered did not differ from the control. Interestingly, functionalization with NeoNectin significantly reduced the attachment of bacteria on the hydrogels. This effect likely stems from an increase in available protonated amine groups of chitosan, as NeoNectin competes with chitosan for reaction with 4-arm PEG-DBCO during crosslinking. It is not clear whether this effect is limiting the attachment or the survival of bacteria, but it is more pronounced for *S. aureus*, whose cell wall is more sensitive to electrostatic interaction with chitosan as explained above.

To further corroborate these findings, an agar diffusion (halo of inhibition) assay was performed after incubating the hydrogels for 24 h on plates containing both bacterial species (Fig. 4C). All hydrogel formulations (CH–N_3, CHN_3–NN, and CHN_3–NNN_3) produced visible inhibition zones, confirming their antibacterial activity through diffusion-mediated effects. Consistent with the live/dead assay, inhibition halos were slightly larger for *S. aureus* than for *P. aeruginosa*, likely reflecting the greater susceptibility of Gram-positive bacteria to the electrostatic disruption induced by chitosan. Importantly, no significant differences were detected among the three hydrogel formulations, indicating that the PEG-azide or NeoNectin modifications did not compromise the intrinsic antimicrobial potential of chitosan.

3.5. MSCs viability, spreading and proliferation

Upon gelation, the hydrogels did not release any cytotoxic component, and MSCs remained highly viable under all tested conditions. Viability consistently exceeded 90% in both indirect contact assays and direct encapsulation experiments (Fig. 5A, B, C), in agreement with previous studies reporting the excellent cytocompatibility of chitosan–PEG hybrid hydrogels (Liu & Chung, 2016).

MSCs encapsulated within the hydrogels exhibited a rounded morphology characteristic of entrapment in a soft 3D environment (Figs. 5D and S3) (Anderson et al., 2011). Interestingly, MSCs progressively adopted a more elongated and spread morphology within the NeoNectin-functionalized hydrogels, as evidenced by a lower circularity ratio compared to the spherical shapes observed in CHN_3 hydrogels (Fig. 5E). This behavior suggests that the α5β1-binding motifs provided by NeoNectin promote integrin-mediated cytoskeletal organization, enhancing cell spreading within the 3D matrix (Robinson et al., n.d.; Yun et al., 2025). Visualization of stress fibers at higher resolution ($> 60\times$) was not possible due to the physical constraints of 3D hydrogel imaging, although this morphological shift is indicative of an early mechanotransductive response, in which integrin clustering triggers downstream signaling through focal adhesion complexes and the reorganization of actin filaments (Sun et al., 2016).

In fact, confocal imaging revealed partial alignment of actin stress fibers along the main elongation axis of the cells in the NeoNectin-containing hydrogels (Fig. 5D). Such behavior has been correlated with enhanced cell–matrix crosstalk and improved differentiation capacity in 3D culture models (Wang et al., 2025).

A marked increase in the cell number was observed in CHN_3-NNN_3 hydrogels, reaching the highest fold-change at day 7 (Fig. 5F). This result underscores the importance of stable protein anchoring for sustaining cell proliferation, as covalent presentation of NeoNectin likely ensures continuous α5β1 integrin engagement and localized signaling. In contrast, most of the non-covalently entrapped NeoNectin in CHN_3–NN hydrogels is released in the first hours, leading to transient rather than sustained stimulation. The progressive increase in cell number observed in covalently NeoNectin-crosslinked systems indicates a favorable balance between hydrogel stability, nutrient diffusion, and integrin-mediated adhesion, key parameters for long-term MSC culture

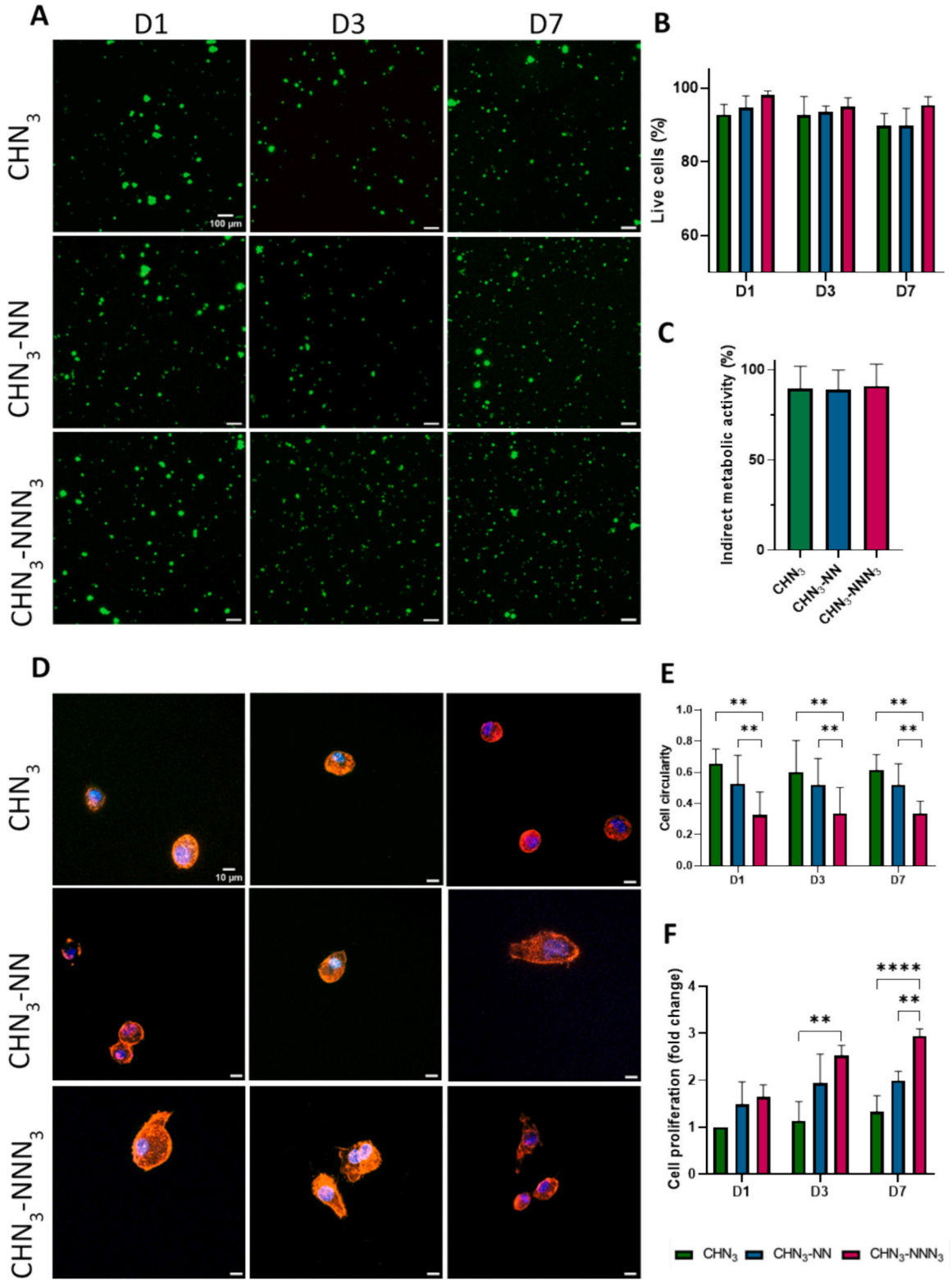

Fig. 5. Response of MSCs encapsulated within chitosan–PEG hydrogels with or without NeoNectin. (A) Live/Dead staining images of encapsulated MSCs at days 1, 3, and 7. Live cells are shown in green and dead cells appear in red. Scale bar denotes 100 µm. (B) Quantification of viable cells expressed as percentage of total cells across different formulations and time points. (C) Metabolic activity of MSCs cultured with conditioned medium from the different hydrogels. The metabolic activity percentage was related to cells cultured in medium without hydrogels. (D) Phalloidin (red) and DAPI (blue) staining of MSCs embedded in the different hydrogel formulations at days 1, 3 and 7. Scale bar denotes 10 µm. (E) Circularity of cells calculated from the phalloidin staining. (F) Cell proliferation of MSCs encapsulated inside the different hydrogels expressed as fold change to CHN_3 at day 1. (For interpretation of the references to color in this figure legend, the reader is referred to the web version of this article.)

in 3D (Gandavarapu et al., 2014).

3.6. MSCs differentiation

To further investigate the osteogenic commitment of MSCs encapsulated within the different hydrogel formulations, early differentiation was evaluated by combining alkaline phosphatase (ALP) activity with the temporal expression of key osteogenic genes (Fig. 6A–C).

RT-qPCR analysis performed at days 3 and 7 revealed a clear temporal and formulation-dependent transcriptional pattern (Fig. 6A–B). At day 3, MSCs encapsulated in CHN_3 hydrogels showed negligible or minimal expression of osteogenic genes, including RUNX2, DLX5, SP7, BMP2, ALP, and OCN. This profile is consistent with the well-established role of soft matrices in maintaining stemness and limiting spontaneous

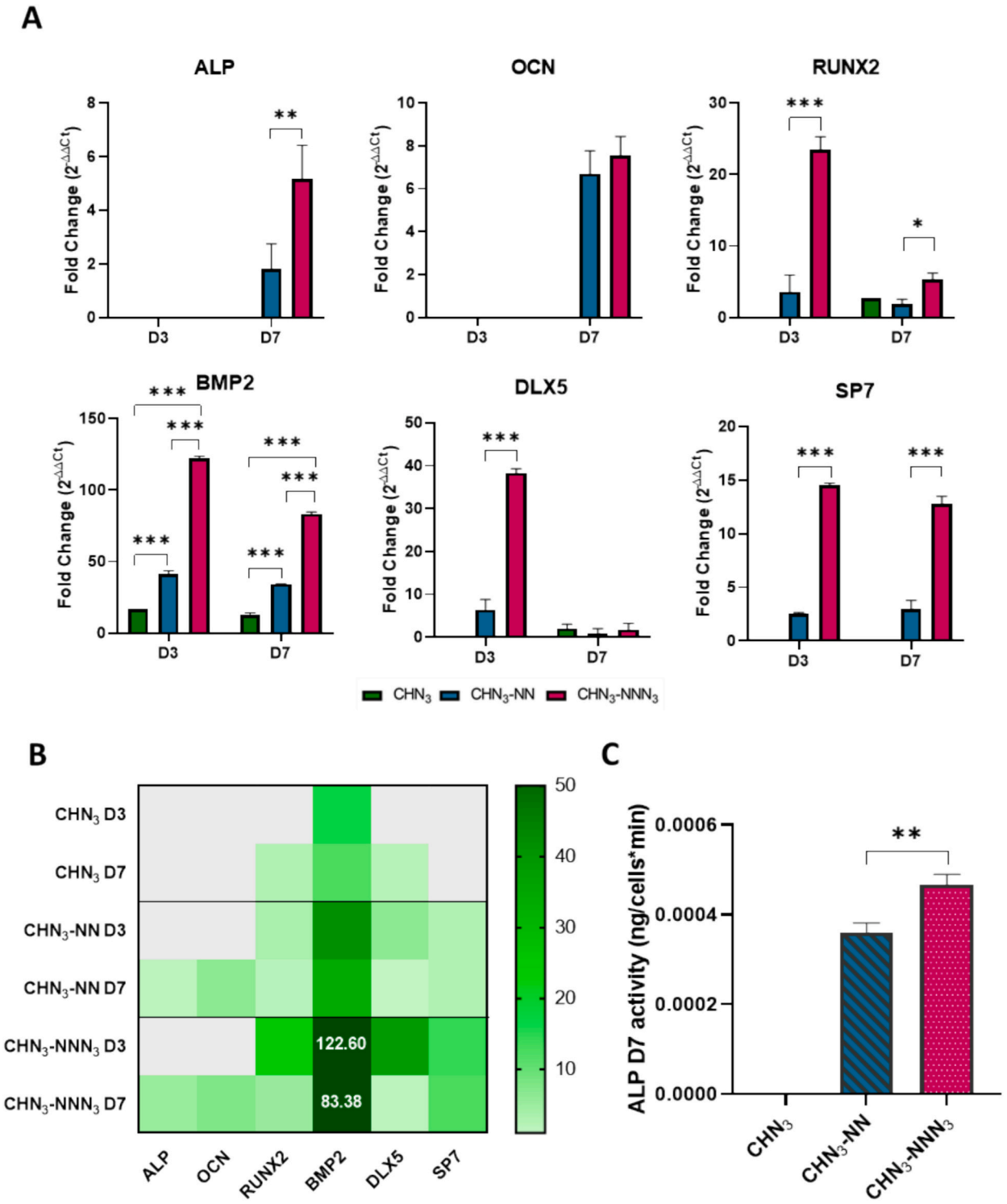

Fig. 6. Differentiation of MSCs encapsulated within chitosan–PEG hydrogels with or without NeoNectin. (A) Expression of ALP, OCN, RUNX2, BMP2, DLX and SP7 genes obtained by RT-qPCR analysis at 3 and 7 days. (B) Heatmap of the studied genes, summarizing the expression of each gene, condition and time point. (C) Early osteogenic differentiation assessed by ALP activity.

osteogenic commitment (El-Rashidy et al., 2021). In contrast, NeoNectin-functionalized hydrogels already induced transcriptional activation of early osteogenic regulators. RUNX2 and DLX5, two upstream transcription factors essential for osteoblast lineage commitment (Lee et al., 2005), were upregulated in CHN_3–NN and more markedly in CHN_3–NNN_3 at day 3. Similarly, SP7, a downstream target of RUNX2 required for osteoblast maturation (Ohba, 2024), followed the same trend. BMP2 expression was also enhanced in NeoNectin-containing matrices, suggesting the initiation of autocrine osteogenic signaling loops (Cai et al., 2020).

By day 7, these differences became more pronounced. CHN_3 hydrogels continued to exhibit minimal osteogenic gene expression, reinforcing the notion that matrix stiffness alone was insufficient to induce differentiation under these conditions. In contrast, CHN_3–NNN_3 displayed the highest expression levels across most markers, including ALP and OCN. The upregulation of OCN, a late-stage osteogenic marker associated with matrix maturation and mineralization (Da Silva Sasso et al., 2023), indicates progression beyond early commitment toward a more differentiated osteoblastic phenotype. CHN_3–NN presented an intermediate transcriptional profile, suggesting that while non-covalently incorporated NeoNectin can initiate early signaling events, sustained presentation through covalent immobilization is required to maintain and amplify osteogenic gene expression over time. The heatmap representation (Fig. 6B) further highlights this temporal progression and clustering of osteogenic gene expression in NeoNectin-containing hydrogels, particularly at day 7, whereas CHN_3 samples remain largely transcriptionally inactive.

After 7 days of culture, ALP activity was detected exclusively in NeoNectin-containing hydrogels (Fig. 6C), indicating early osteogenic commitment of MSCs in response to α5β1-specific engagement. Although most NeoNectin in the CHN_3–NN formulation should have been released shortly after gelation, its high affinity for α5β1 likely limited premature loss during initial cell encapsulation and before hydrogel gelation, enabling localized integrin clustering and osteogenic signaling (Oh et al., 2017). Notably, covalently immobilized NeoNectin within CHN_3–NNN_3 hydrogels produced a significantly higher ALP signal, highlighting the importance of stable crosslinked presentation for promoting osteogenic differentiation. These findings are consistent with previous reports demonstrating that persistent integrin–ligand interactions promote activation of downstream signaling pathways such as FAK, ERK1/2, and RUNX2, ultimately leading to enhanced ALP expression and matrix mineralization (Liu et al., 2023).

Importantly, these effects cannot be attributed to differences in matrix mechanics. All hydrogel formulations displayed comparable viscoelastic properties within a soft mechanical range typically associated with stem cell maintenance and within the physiological stiffness range of bone marrow as discussed before, where MSCs are expected to remain undifferentiated. Consistent with this, MSCs did not differentiate in CHN_3 hydrogels, in which stiffness remained below the threshold generally required to promote osteogenic differentiation (El-Rashidy et al., 2021). Therefore, the absence of osteogenic markers and ALP activity in CHN_3 confirms that matrix stiffness alone is insufficient to trigger differentiation in this system, so the observed differences in MSC proliferation and differentiation can be attributed to the biochemical presentation of NeoNectin rather than to variations in stiffness. By maintaining constant matrix mechanics, this platform effectively decouples biochemical and mechanical cues, enabling precise evaluation of α5β1-specific engagement within a controlled 3D microenvironment. Only NeoNectin-functionalized matrices, particularly the covalently immobilized CHN_3–NNN_3 condition, elicited robust activation of osteogenic transcription factors and functional differentiation markers, indicating that specific integrin engagement can override mechanical permissiveness and drive osteogenic commitment in an ultra-soft environment (Zhang et al., 2021).

4. Conclusions

This work presents an innovative strategy to engineer multifunctional chitosan-based hydrogels by integrating SPAAC click chemistry with de novo–designed integrin-binding proteins. The resulting NeoNectin-functionalized hydrogels exhibit excellent mechanical stability, high water retention, controlled degradation rate and strong antibacterial activity while maintaining full cytocompatibility. Importantly, the incorporation of NeoNectin does not substantially alter the viscoelastic properties of the network, confirming that the observed differences in cell proliferation and differentiation arise from specific biochemical signaling rather than mechanical effects.

By coupling advanced polymer chemistry with protein engineering, this study demonstrates how the precise spatial presentation of bioactive ligands within a mechanically robust hydrogel can direct stem cell behavior in 3D. The observed degradation profiles confirm the suitability of these hydrogels as dynamically remodelable matrices, ensuring that they provide a stable structural scaffold while gradually allowing the formation of new bone when implanted. The modularity and biorthogonal design of this system make it a promising platform for bone regeneration and broader applications in regenerative medicine, where the combination of structural integrity and biochemical specificity is essential for clinical translation.

From a clinical perspective, the rapid and catalyst-free gelation of the SPAAC-functionalized chitosan network enables a minimally invasive implantation strategy. As an injectable, in situ forming system, the hydrogel can adapt to the complex geometries of irregular bone voids, providing an immediate antimicrobial barrier while recruiting endogenous cells. These findings suggest that NeoNectin-functionalized hydrogels may be particularly relevant for regenerative strategies involving marrow-containing defects or injectable biomaterials, where the surrounding microenvironment remains mechanically soft during early stages of healing, although requires precise biochemical signaling to ensure successful osteogenesis.

CRediT authorship contribution statement

Daniel Cabrerizo-Aguado: Writing – review & editing, Writing – original draft, Methodology, Investigation, Formal analysis, Data curation. **Federica Barbugian:** Writing – review & editing, Writing – original draft, Methodology, Investigation, Formal analysis, Data curation. **Maria-Pau Ginebra:** Writing – review & editing, Writing – original draft, Resources, Project administration, Funding acquisition. **Xinru Wang:** Writing – review & editing, Writing – original draft, Validation, Methodology, Investigation, Formal analysis, Conceptualization. **David Baker:** Writing – review & editing, Writing – original draft, Validation, Supervision, Resources, Project administration, Investigation, Funding acquisition, Conceptualization. **Jose Maria Manero:** Writing – review & editing, Writing – original draft, Supervision, Resources, Project administration, Funding acquisition, Conceptualization. **Jordi Guillem-Marti:** Writing – review & editing, Writing – original draft, Validation, Supervision, Resources, Project administration, Methodology, Funding acquisition, Data curation, Conceptualization.

Declaration of competing interest

The authors declare the following financial interests/personal relationships which may be considered as potential competing interests: Jordi Guillem-Marti, Xinru Wang and David Baker are co-inventors on the provisional patent #De Novo Designed alpha(5) beta(1) Integrin selective minibinders (US20240383964A1) filed by the University of Washington. X.W. and D.B. are co-founders of Lila Biologics and own stock or stock options in the company. The other authors declare that they have no known competing financial interests or personal relationships that could have appeared to influence the work reported in this paper.

Acknowledgements

This work has received funding from the Spanish Government MICIU /AEI /10.13039/501100011033 / FEDER, UE through project PID2024-160637OB-I00, co-funded by the EU through the European Regional Development Funds. J.G.-M. acknowledges the Ramon y Cajal grant (RYC2022-038006-I) from the Spanish State Research Agency and the European Union Next Generation, EU, Ministry of Science, Innovation and Universities and Recovery, Transformation and Resilience Plan MCIN/AEI/10.13039/501100011033. X. W. and D.B. acknowledge the Audacious project, the Defense Threat Reduction Agency grant HDTRA1-21-1-0007 and the Nordstrom Barrier Institute for Protein Design Directors Fund. This work is part of Maria de Maeztu Units of Excellence Programme CEX2023-001300-M / funded by MCIN/AEI /10.13039/501100011033. D.C.-A. acknowledges the Predoctoral program AGAUR-FI (2024 FI-1 00198) Joan Oró and M.-P.G. the ICREA Academia award, both funded by the Generalitat of Catalunya, and the European Social Plus Fund. The authors would like to thank Tània Vilella and Raúl Agut for their support in mechanical characterization experiments.

Appendix A. Supplementary data

Supplementary data to this article can be found online at https://doi.org/10.1016/j.carbpol.2026.125392.

Data availability

Data will be made available on request.

References

Ai, X., Lyu, L., Mu, J., Hu, M., Wang, Z., & Xing, B. (2017). Synthesis of core-shell lanthanide-doped upconversion nanocrystals for cellular applications. *Journal of Visualized Experiments*. , Article 56416. https://doi.org/10.3791/56416

Anderson, S. B., Lin, C.-C., Kuntzler, D. V., & Anseth, K. S. (2011). The performance of human mesenchymal stem cells encapsulated in cell-degradable polymer-peptide hydrogels. *Biomaterials, 32*, 3564–3574. https://doi.org/10.1016/j.biomaterials.2011.01.064

Bellis, S. L. (2011). Advantages of RGD peptides for directing cell association with biomaterials. *Biomaterials, 32*, 4205–4210. https://doi.org/10.1016/j.biomaterials.2011.02.029

Boni, R., & Regan, L. (2023). Modulating the viscoelastic properties of covalently crosslinked protein hydrogels. *gels, 9*, 481. https://doi.org/10.3390/gels9060481

Branco, M. C., Pochan, D. J., Wagner, N. J., & Schneider, J. P. (2010). The effect of protein structure on their controlled release from an injectable peptide hydrogel. *Biomaterials, 31*, 9527–9534. https://doi.org/10.1016/j.biomaterials.2010.08.047

Cai, H., Zou, J., Wang, W., & Yang, A. (2020). BMP2 induces hMSC osteogenesis and matrix remodeling. *Molecular Medicine Reports, 23*, 125. https://doi.org/10.3892/mmr.2020.11764

Chang, F.-C., Tsao, C.-T., Lin, A., Zhang, M., Levengood, S., & Zhang, M. (2016). PEG-chitosan hydrogel with tunable stiffness for study of drug response of breast cancer cells. *Polymers, 8*, 112. https://doi.org/10.3390/polym8040112

Cheng, B., Pei, B., Wang, Z., & Hu, Q. (2017). Advances in chitosan-based superabsorbent hydrogels. *RSC Advances, 7*, 42036–42046. https://doi.org/10.1039/C7RA07104C

Da Silva Sasso, G. R., Florencio-Silva, R., De Pizzol-Júnior, J. P., Gil, C. D., Simões, M. D. J., Sasso-Cerri, E., & Cerri, P. S. (2023). Additional insights into the role of osteocalcin in osteoblast differentiation and in the early steps of developing alveolar process of rat molars. *The Journal of Histochemistry and Cytochemistry, 71*, 689–708. https://doi.org/10.1369/00221554231211630

Day, G. J., Zhang, Q., Remillat, C. D. L., Comandini, G., Perriman, A. W., & Scarpa, F. (2025). Tunable network architecture in a hydrogel with extreme vibration damping properties. *Communications Materials, 6*, 148. https://doi.org/10.1038/s43246-025-00857-5

Delgado, M., Spanka, C., Kerwin, L. D., Wentworth, P., & Janda, K. D. (2002). A tunable hydrogel for encapsulation and controlled release of bioactive proteins. *Biomacromolecules, 3*, 262–271. https://doi.org/10.1021/bm010147y

Doherty-Boyd, W. S., Tsimbouri, P. M., Jayawarna, V., Walker, M., Taqi, A. F., Mahon, N., Meek, D., Young, P., Miller, A., West, A., Salmeron-Sanchez, M., Dalby, M. J., & Donnelly, H. (2025). Synthetic peptide hydrogels as a model of the bone marrow niche demonstrate efficacy of a combined CRISPR-CAR T-cell therapy for acute myeloid leukaemia. *Biomaterials*. , Article 123803. https://doi.org/10.1016/j.biomaterials.2025.123803

Dong, Q., Xiong, S., Dong, X., Tang, Y., Dai, X., Chen, P., & Zhang, Z. (2026). Light-activated chitosan hydrogel: A bioadhesive platform for emergency hemostasis and bacteria-infected wound management. *Carbohydrate Polymers, 372*, Article 124557. https://doi.org/10.1016/j.carbpol.2025.124557

Donnelly, H., Ross, E., Xiao, Y., Hermantara, R., Taqi, A. F., Doherty-Boyd, W. S., … Dalby, M. J. (2024). Bioengineered niches that recreate physiological extracellular matrix organisation to support long-term haematopoietic stem cells. *Nature Communications, 15*, Article 5791. https://doi.org/10.1038/s41467-024-50054-0

Drápalová, E., Michlovská, L., Poštulková, H., Chamradová, I., Lipový, B., Holoubek, J., Vacek, L., Růžička, F., Hanslianová, M., Svobodová, T., Černá, E., Hrdličková, B., & Vojtová, L. (2023). Antimicrobial cost-effective transparent hydrogel films from renewable gum karaya/chitosan polysaccharides for modern wound dressings. *ACS Applied Polymer Materials, 5*(4), 2774–2786. https://doi.org/10.1021/acsapm.3c00025

Elmengaard, B., Bechtold, J. E., & Søballe, K. (2005). In vivo study of the effect of RGD treatment on bone ongrowth on press-fit titanium alloy implants. *Biomaterials, 26*, 3521–3526. https://doi.org/10.1016/j.biomaterials.2004.09.039

El-Rashidy, A. A., El Moshy, S., Radwan, I. A., Rady, D., Abbass, M. M. S., Dörfer, C. E., & Fawzy El-Sayed, K. M. (2021). Effect of polymeric matrix stiffness on osteogenic differentiation of mesenchymal stem/progenitor cells: Concise review. *Polymers, 13*, Article 2950. https://doi.org/10.3390/polym13172950

Fan, M., Ma, Y., Mao, J., Zhang, Z., & Tan, H. (2015). Cytocompatible in situ forming chitosan/hyaluronan hydrogels via a metal-free click chemistry for soft tissue engineering. *Acta Biomaterialia, 20*, 60–68. https://doi.org/10.1016/j.actbio.2015.03.033

Freier, T., Koh, H. S., Kazazian, K., & Shoichet, M. S. (2005). Controlling cell adhesion and degradation of chitosan films by N-acetylation. *Biomaterials, 26*, 5872–5878. https://doi.org/10.1016/j.biomaterials.2005.02.033

Fu, S., Dong, H., Deng, X., Zhuo, R., & Zhong, Z. (2017). Injectable hyaluronic acid/poly (ethylene glycol) hydrogels crosslinked via strain-promoted azide-alkyne cycloaddition click reaction. *Carbohydrate Polymers, 169*, 332–340. https://doi.org/10.1016/j.carbpol.2017.04.028

Gandavarapu, N. R., Alge, D. L., & Anseth, K. S. (2014). Osteogenic differentiation of human mesenchymal stem cells on α5 integrin binding peptide hydrogels is dependent on substrate elasticity. *Biomaterials Science, 2*, 352–361. https://doi.org/10.1039/C3BM60149H

Genshaft, A., Moser, J. S., D'Antonio, E. L., Bowman, C. M., & Christianson, D. W. (2013). Energetically unfavorable amide conformations for N6-acetyllysine side chains in refined protein structures. *Proteins, 81*, 1051–1057. https://doi.org/10.1002/prot.24262

Gómez-Fernández, J. C., & Villalaín, J. (1998). The use of FT-IR for quantitative studies of the apparent pKa of lipid carboxyl groups and the dehydration degree of the phosphate group of phospholipids. *Chemistry and Physics of Lipids, 96*, 41–52. https://doi.org/10.1016/S0009-3084(98)00079-6

Hagan, R. M., Björnsson, R., McMahon, S. A., Schomburg, B., Braithwaite, V., Bühl, M., … Schwarz-Linek, U. (2010). NMR spectroscopic and theoretical analysis of a spontaneously formed Lys–Asp isopeptide bond. *Angewandte Chemie, International Edition, 49*, 8421–8425. https://doi.org/10.1002/anie.201004340

Han, S.-S., Yoon, H. Y., Yhee, J. Y., Cho, M. O., Shim, H.-E., Jeong, J.-E., … Kang, S.-W. (2018). In situ cross-linkable hyaluronic acid hydrogels using copper free click chemistry for cartilage tissue engineering. *Polymer Chemistry, 9*, 20–27. https://doi.org/10.1039/C7PY01654A

Hodgson, S. M., Bakaic, E., Stewart, S. A., Hoare, T., & Adronov, A. (2016). Properties of poly(ethylene glycol) hydrogels cross-linked via strain-promoted alkyne–azide cycloaddition (SPAAC). *Biomacromolecules, 17*, 1093–1100. https://doi.org/10.1021/acs.biomac.5b01711

Hong, F., Qiu, P., Wang, Y., Ren, P., Liu, J., Zhao, J., & Gou, D. (2024). Chitosan-based hydrogels: From preparation to applications, a review. *Food Chemistry: X, 21*, Article 101095. https://doi.org/10.1016/j.fochx.2023.101095

Huan, Y., Kong, Q., Mou, H., & Yi, H. (2020). Antimicrobial peptides: Classification, design, application and research progress in multiple fields. *Frontiers in Microbiology, 11*, Article 582779. https://doi.org/10.3389/fmicb.2020.582779

Huynh, N.-T., Jeon, Y.-S., Kim, D., & Kim, J.-H. (2013). Preparation and swelling properties of "click" hydrogel from polyaspartamide derivatives using tri-arm PEG and PEG-co-poly(amino urethane) azides as crosslinking agents. *Polymer, 54*, 1341–1349. https://doi.org/10.1016/j.polymer.2013.01.001

Ikeda, T. (2018). Glycidyl triazolyl polymers: Poly(ethylene glycol) derivatives functionalized by azide–alkyne cycloaddition reaction. *Macromolecular Rapid Communications, 39*, Article 1700825. https://doi.org/10.1002/marc.201700825

Ji, Y., Yang, X., Ji, Z., Zhu, L., Ma, N., Chen, D., Jia, X., Tang, J., & Cao, Y. (2020). DFT-calculated IR spectrum amide I, II, and III band contributions of N -methylacetamide fine components. *ACS Omega, 5*, 8572–8578. https://doi.org/10.1021/acsomega.9b04421

Jiang, Y., Hu, A., Feng, W., Chen, Y., Ai, M., Yu, D., & Wang, W. (2024). Non-covalent crosslinked hydrogels to realize renewable and re-moldable strain sensors with excellent sensing behavior. *Polymer, 290*, Article 126588. https://doi.org/10.1016/j.polymer.2023.126588

Ke, C.-L., Deng, F.-S., Chuang, C.-Y., & Lin, C.-H. (2021). Antimicrobial actions and applications of chitosan. *polymers, 13*, 904. https://doi.org/10.3390/polym13060904

Khetan, S., & Burdick, J. A. (2011). Patterning hydrogels in three dimensions towards controlling cellular interactions. *Soft Matter, 7*, 830–838. https://doi.org/10.1039/C0SM00852D

Kovács, R., Erdélyi, L., Fenyvesi, F., Balla, N., Kovács, F., Vámosi, G., Klusóczki, Á., Gyöngyösi, A., Bácskay, I., Vecsernyés, M., & Váradi, J. (2022). Concentration-dependent antibacterial activity of chitosan on Lactobacillus plantarum. *Pharmaceutics, 15*, 18. https://doi.org/10.3390/pharmaceutics15010018

Kuboki, T., & Kidoaki, S. (2025). Surface-elastic hydrogels delay senescence via the modulation of redox homeostasis and cytoskeletal tension. *Scientific Reports, 15*, 20460. https://doi.org/10.1038/s41598-025-04779-7

Kwon, S., Choi, H., Park, C., Choi, S., Kim, E., Kim, S. W., … Koo, H. (2021). In vivo vocal fold augmentation using an injectable polyethylene glycol hydrogel based on click chemistry. *Biomaterials Science, 9*, 108–115. https://doi.org/10.1039/D0BM01155J

Lee, M.-H., Kim, Y.-J., Yoon, W.-J., Kim, J.-I., Kim, B.-G., Hwang, Y.-S., Wozney, J. M., Chi, X.-Z., Bae, S.-C., Choi, K.-Y., Cho, J.-Y., Choi, J.-Y., & Ryoo, H.-M. (2005). Dlx5 specifically regulates Runx2 type II expression by binding to homeodomain-response elements in the Runx2 distal promoter. *Journal of Biological Chemistry, 280*, 35579–35587. https://doi.org/10.1074/jbc.M502267200

Li, X., Liu, Y., Wong, E. C. N., & Winnik, M. A. (2025). NMR studies of PEG chain dynamics on mesoporous silica nanoparticles for minimizing non-specific binding. *Nanoscale, 17*, 14759–14771. https://doi.org/10.1039/D5NR00936G

Li, X., & Xiong, Y. (2022). Application of "click" chemistry in biomedical hydrogels. *ACS Omega, 7*, 36918–36928. https://doi.org/10.1021/acsomega.2c03931

Liu, H., & Chung, H. (2016). Self-healing properties of lignin-containing nanocomposite: Synthesis of lignin- graft -poly(5-acetylaminopentyl acrylate) via RAFT and click chemistry. *Macromolecules, 49*, 7246–7256. https://doi.org/10.1021/acs.macromol.6b01028

Liu, X., Ye, Y., Li, Z., Liao, L., & Wei, Q. (2026). Mechanical rejuvenation of senescent stem cells and aged bone via chromatin remodeling. *Nature Communications, 17*, 1684. https://doi.org/10.1038/s41467-026-68387-3

Liu, Z., Wang, Q., Zhang, J., Qi, S., Duan, Y., & Li, C. (2023). The mechanotransduction signaling pathways in the regulation of osteogenesis. *IJMS, 24*, Article 14326. https://doi.org/10.3390/ijms241814326

Lv, X., Liu, C., Shao, Z., & Sun, S. (2019). Tuning physical crosslinks in hybrid hydrogels for network structure analysis and mechanical reinforcement. *polymers, 11*, 352. https://doi.org/10.3390/polym11020352

Madl, C. M., Katz, L. M., & Heilshorn, S. C. (2016). Bio-orthogonally crosslinked, engineered protein hydrogels with tunable mechanics and biochemistry for cell encapsulation. *Advanced Functional Materials, 26*, 3612–3620. https://doi.org/10.1002/adfm.201505329

Nealy, E. S., Reed, S. J., Adelmund, S. M., Badeau, B. A., Shadish, J. A., Girard, E. J., Brasel, K., Pakiam, F. J., Mhyre, A. J., Price, J. P., Sarkar, S., Kalia, V., DeForest, C. A., & Olson, J. M. (2024). Versatile tissue-injectable hydrogels capable of the extended hydrolytic release of bioactive protein therapeutics. *Bioengineering & Translational Medicine, 9*, Article e10668. https://doi.org/10.1002/btm2.10668

Nicolle, L., Journot, C. M. A., & Gerber-Lemaire, S. (2021). Chitosan functionalization: Covalent and non-covalent interactions and their characterization. *Polymers, 13*, 4118. https://doi.org/10.3390/polym13234118

Oh, S.-H., Kim, J.-W., Kim, Y., Lee, M. N., Kook, M.-S., Choi, E. Y., Im, S.-Y., & Koh, J.-T. (2017). The extracellular matrix protein Edil3 stimulates osteoblast differentiation through the integrin α5β1/ERK/Runx2 pathway. *PLoS ONE, 12*, Article e0188749. https://doi.org/10.1371/journal.pone.0188749

Ohba, S. (2024). Regulatory landscape of Runx2 and Sp7 in osteoblast and chondrocyte lineages: Recent findings from next-generation sequencer-based studies. *Oral Science International, 21*, 28–36. https://doi.org/10.1002/osi2.1184

Patten, J., & Wang, K. (2021). Fibronectin in development and wound healing. *Advanced Drug Delivery Reviews, 170*, 353–368. https://doi.org/10.1016/j.addr.2020.09.005

Ramya, K., Shanmugam, R., Latha, S., Sahana, R., Mounica, P., Elangovan, A., & Arivazhagan, G. (2024). Self-associates of 1,2,4-triazole: FTIR studies, quantum chemical calculations and topological analysis. *Journal of Molecular Structure, 1316*, Article 138926. https://doi.org/10.1016/j.molstruc.2024.138926

Rayamajhi, S., & Aryal, S. (2020). Surface functionalization strategies of extracellular vesicles. *Journal of Materials Chemistry B, 8*, 4552–4569. https://doi.org/10.1039/D0TB00744G

Robinson, E.E., Foty, R.A., Corbett, S.A., n.d. Fibronectin matrix assembly regulates 5 1-mediated cell cohesion.

Rodrigues, S., Dionísio, M., López, C. R., & Grenha, A. (2012). Biocompatibility of chitosan carriers with application in drug delivery. *JFB, 3*, 615–641. https://doi.org/10.3390/jfb3030615

Rolón-Garrido, V. H., & Wagner, M. H. (2009). The damping function in rheology. *Rheologica Acta, 48*, 245–284. https://doi.org/10.1007/s00397-008-0308-x

Sajeev, D., Rajesh, A., Nethish Kumaar, R., Aswin, D., Jayakumar, R., & Nair, S. C. (2025). Chemically modified chitosan as a functional biomaterial for drug delivery system. *Carbohydrate Research, 548*, Article 109351. https://doi.org/10.1016/j.carres.2024.109351

Segneanu, A.-E., Bejenaru, L. E., Bejenaru, C., Blendea, A., Mogoşanu, G. D., Biță, A., & Boia, E. R. (2025). Advancements in hydrogels: A comprehensive review of natural and synthetic innovations for biomedical applications. *Polymers, 17*, Article 2026. https://doi.org/10.3390/polym17152026

Sizeland, K. H., Hofman, K. A., Hallett, I. C., Martin, D. E., Potgieter, J., Kirby, N. M., Hawley, A., Mudie, S. T., Ryan, T. M., Haverkamp, R. G., & Cumming, M. H. (2018). Nanostructure of electrospun collagen: Do electrospun collagen fibers form native structures? *Materialia, 3*, 90–96. https://doi.org/10.1016/j.mtla.2018.10.001

Stagi, L., Sini, M., Carboni, D., Anedda, R., Siligardi, G., Gianga, T.-M., … Innocenzi, P. (2022). Modulating the poly-l-lysine structure through the control of the protonation–deprotonation state of l-lysine. *Scientific Reports, 12*, 19719. https://doi.org/10.1038/s41598-022-24109-5

Stojkov, G., Niyazov, Z., Picchioni, F., & Bose, R. K. (2021). Relationship between structure and rheology of hydrogels for various applications. *Gels, 7*, 255. https://doi.org/10.3390/gels7040255

Sun, Z., Guo, S. S., & Fässler, R. (2016). Integrin-mediated mechanotransduction. *Journal of Cell Biology, 215*, 445–456. https://doi.org/10.1083/jcb.201609037

Sutton, J. A. F., Carnell, O. T., Lafage, L., Gray, J., Biboy, J., Gibson, J. F., … Foster, S. J. (2021). Staphylococcus aureus cell wall structure and dynamics during host-pathogen interaction. *PLoS Pathogens, 17*, Article e1009468. https://doi.org/10.1371/journal.ppat.1009468

Tang, J., Li, Y., Song, Y., Wu, X., Yu, G., & Tam, K. C. (2020). Carbodiimide coupling versus click chemistry for nanoparticle surface functionalization: A comparative study for the encapsulation of sodium cholate by cellulose nanocrystals modified with β-cyclodextrin. *Carbohydrate Polymers, 244*, Article 116512. https://doi.org/10.1016/j.carbpol.2020.116512

Thi, M. T. T., Wibowo, D., & Rehm, B. H. A. (2020). *Pseudomonas aeruginosa* biofilms. *IJMS, 21*, Article 8671. https://doi.org/10.3390/ijms21228671

Tibbitt, M. W., & Anseth, K. S. (2009). Hydrogels as extracellular matrix mimics for 3D cell culture. *Biotechnology and Bioengineering, 103*, 655–663. https://doi.org/10.1002/bit.22361

Truong, V. X., Ablett, M. P., Gilbert, H. T. J., Bowen, J., Richardson, S. M., Hoyland, J. A., & Dove, A. P. (2014). In situ-forming robust chitosan-poly(ethylene glycol) hydrogels prepared by copper-free azide–alkyne click reaction for tissue engineering. *Biomaterials Science, 2*, 167–175. https://doi.org/10.1039/C3BM60159E

Tsao, C. T., Hsiao, M. H., Zhang, M. Y., Levengood, S. L., & Zhang, M. (2015). Chitosan-PEG hydrogel with sol-gel transition triggerable by multiple external stimuli. *Macromolecular Rapid Communications, 36*, 332–338. https://doi.org/10.1002/marc.201400586

Wang, X., Guillem-Marti, J., Kumar, S., Lee, D. S., Cabrerizo-Aguado, D., Werther, R., Alamo, K. A. E., Zhao, Y. T., Nguyen, A., Kopyeva, I., Huang, B., Li, J., Hao, Y., Li, X., Brizuela-Velasco, A., Murray, A., Gerben, S., Roy, A., DeForest, C. A., … Baker, D. (2025). De novo design of integrin α5β1 modulating proteins to enhance biomaterial properties. *Advanced Materials, 37*, Article 2500872. https://doi.org/10.1002/adma.202500872

Yun, Y. G., Heo, S. C., Jung, J.-W., Yeo, D., Shin, S.-J., Tsogtbaatar, K., Hwang, Y., Lee, J.-H., Lee, J. H., & Kim, H.-W. (2025). Mechanosignaling and 3D morphological adaptation of MSCs in response to hydrogel rigidity underpin angiogenic and immunomodulatory efficacy for ischemic injury regeneration. *Bioactive Materials, 53*, 404–416. https://doi.org/10.1016/j.bioactmat.2025.07.027

Zhang, M., Sun, Q., Liu, Y., Chu, Z., Yu, L., Hou, Y., Kang, H., Wei, Q., Zhao, W., Spatz, J. P., Zhao, C., & Cavalcanti-Adam, E. A. (2021). Controllable ligand spacing stimulates cellular mechanotransduction and promotes stem cell osteogenic differentiation on soft hydrogels. *Biomaterials, 268*, Article 120543. https://doi.org/10.1016/j.biomaterials.2020.120543

Zöller, K., To, D., & Bernkop-Schnürch, A. (2025). Biomedical applications of functional hydrogels: Innovative developments, relevant clinical trials and advanced products. *Biomaterials, 312*, Article 122718. https://doi.org/10.1016/j.biomaterials.2024.122718